A Multi-Physics Finite Element Analysis of Round Pin High Power Connectors

by

John Robert Polchow

A thesis submitted to the Graduate Faculty of
Auburn University
in partial fulfillment of the
requirements for the Degree of
Master of Science

Auburn, Alabama
May 14, 2010

Keywords: multiscale properties, rough surface contact, finite element modeling

Approved by

Robert L. Jackson, Chair, Associate Professor of Mechanical Engineering
Song-yul Choe, Associate Professor of Mechanical Engineering
George T. Flowers, Professor of Mechanical Engineering

Abstract

In the past decade, the general public's means of transportation has begun to undergo a radical transformation, moving away from only using gasoline and moving toward using a combination of gasoline and electricity. This switch will depend on a number of parameters, including the cost, the availability, and the possible health and environmental effects of gasoline. However, these are not the only mechanisms driving the debate. The cost and feasibility of mass producing a reliable electric vehicle will also help to determine its popularity on the market. The paradigm by which the motor vehicle is viewed may need to change radically before the electric vehicle can totally take over the transportation needs of a country like the United States. One parameter that shouldn't stand in the way is the overall reliability of the electric vehicle, which is dependent upon the electric connections between the power source and the motor.

Contact degradation in the electric connector, caused by fretting, occurs as a result of relative motion between two surfaces, which can be caused by vibration, thermal cycling, electric cycling, etc. This degradation, which decreases the performance of the contact by adding resistance, needs to be minimized and then controlled in order to increase the operating lifetime of the connector. By understanding the fundamental multi-physics mechanisms that cause fretting, better connectors can be designed, built, and implemented in any number of applications, including automotive, manufacturing, and microelectronic industries. Using a commercial multi-physics finite element software package, a model, incorporating multiscale properties, such as electrical contact resistance and thermal contact resistance, was constructed to

predict the behavior of the round pin, high power connector under normal operating conditions. As a way to test the validity of the model, an experiment was devised to measure connector resistance and temperature along the surface of the connector. The theoretical results were correlated with the experimental results and showed the same trends. The multiscale contact resistance was artificially increased by several factors as a way to show how the connector may perform under fretting conditions. The model predicts an increase in connector resistance and temperature for both increasing current and increasing electrical contact resistance. The model also shows, for increasing current and increasing electrical contact resistance, that current becomes more concentrated along the path it travels in and out of the connector. This constriction of current, most likely due to the connector geometry, could lead to much higher surface temperatures than the model currently predicts, resulting in thermally induced softening or distortion in the connector.

Acknowledgments

The author would like to acknowledge and thank especially the members of his research committee, Dr. Robert L. Jackson, Dr. Song-yul Choe, and Dr. George T. Flowers, for their advice and support on this project, without which, this project would have proven infinitely more difficult. The author would also like to thank L.S. Cable for their contributions to the project. Finally, the author would like to thank Mr. Rujian Fu and Mr. Stephen Wall for their dedication and resourcefulness in the lab, which contributed to this project's overall fundamental understanding of connector reliability.

Table of Contents

List of Tables

List of Figures

List of Abbreviations

ε_r	strain in the radial direction (cylindrical coordinates)
σ_r	stress normal to the radial direction (cylindrical coordinates)
ν	Poisson's ratio
σ_θ	stress normal to the θ direction (cylindrical coordinates)
σ_z	stress normal to the z direction(cylindrical coordinates)
α	coefficient of thermal expansion
ΔT	change in temperature
ε_θ	strain in the θ direction (cylindrical coordinates)
ε_z	strain in the z direction (cylindrical coordinates)
$\gamma_{r\theta}$	shear strain in the $r\theta$ plane (cylindrical coordinates)
E	elastic modulus
$\tau_{r\theta}$	shear stress in the $r\theta$ plane (cylindrical coordinates)
γ_{rz}	shear strain in the rz plane (cylindrical coordinates)
τ_{rz}	shear stress in the rz plane (cylindrical coordinates)
$\gamma_{\theta z}$	shear strain in the θz plane (cylindrical coordinates)
$\tau_{\theta z}$	shear stress in the θz plane (cylindrical coordinates)
I	electric current

σ	electrical conductivity
∇	gradient operator
Φ	electric potential field
Q	heat
k	thermal conductivity
T	temperature field
ρ	electric resistivity
ECR	electrical contact resistance
R	electrical resistance
N	number of circular contact spots
α	radius of cluster of contact spots
A	area
f	spatial frequency (reciprocal of wavelength)
$\overline{p}$	mean pressure
p^*	average pressure for complete contact
E'	$E/(1-\nu^2)$
Δ	asperity amplitude
C	critical yield stress coefficient
S_y	yield strength
A_c	critical area at transition from elastic to plastic regime
$\overline{p}_c$	critical average pressure over nominal area at transition from elastic to plastic regime
A_p	contact area in the plastic regime
A	contact area

$\overline{A}$	individual asperity area of contact
η	asperity density
A_n	nominal area of contact
P	contact force
$\overline{P}$	individual asperity contact force
a	radius of the area of contact
Ψ_i	alleviation factor
R_a	average roughness
R_q	root mean square roughness, standard deviation of roughness
z	distance of asperity measured from the leveled surface height

Subscripts

E	elastic regime
P	plastic regime
c	critical value at onset of plastic deformation
i	frequency level
JGH	from Johnson, Greenwood, and Higginson model

CHAPTER 1

Introduction

All motor vehicles are subject to a wide range of conditions depending on how the operator drives. Impulses that act upon the vehicle will elicit a mechanical response in the form of vibrations. Fuel injected motors, which utilize hydrocarbons, are relatively immune to these vibrations, as they should be insufficient to adversely affect the overall performance and operating lifetime of the vehicle. Electric motors, on the other hand, require appropriate electrical connectors to supply power from the power source. Mechanical vibrations that a car undergoes while in transit will shorten the operating lifetime of these electrical connectors. As these connectors are vibrated, the contacts fret, leading to an increase in electrical resistance. As electrical resistance increases at constant voltage, current decreases, thus decreasing the power supplied to the motor until the motor no longer functions or cannot be controlled properly.

The effort to study fretting of electrical connectors can be done through the lenses of mechanical engineering, electrical engineering, materials engineering, and physics. Research has found that contact resistance of electrical connectors is dominated by the materials, tribology, and dynamics of the system [1-12]. Efforts to model all of these factors concurrently have been minimal to date. The need remains to include such factors as material properties, contact geometry, vibration frequency, displacement amplitude, electric current, and ambient conditions into a comprehensive model, which could be used to predetermine the operating lifetime of an electrical connector.

The current work approaches the problem of contact resistance in electrical connectors by measuring the surface of the electrical connector using a stylus

profilometer. The electrical and thermal contact resistances may be calculated as a function of pressure using the multiscale method described in Wilson et al. [13] and included in the steady-state, multi-physics finite element analysis on the round pin, high power electrical connector, yielding the electrical contact resistance, temperature distribution, stress, and current density as functions of current. Finally, these theoretical results will be compared to the experimental results collected from powering the round pin connector at incremental amperages. In an effort to simulate the behavior of the connector under fretting conditions, electrical contact resistance as calculated by the multiscale method, described in Wilson et al. [13], was increased on a percentage basis and included in the steady-state, multi-physics finite element analysis, yielding the electrical contact resistance, temperature distribution, stress, and current density as functions of percent increase of electrical contact resistance.

CHAPTER 2

Background and Literature Review

Electrical contact resistance, simply put, is the electrical resistance current faces when going from one surface to another surface. All engineering surfaces are rough at some scale. When two surfaces are in contact with each other, only a small fraction of the surfaces are in contact with each other, and these points of contact occur at the asperities, or "highest tips" of the surfaces. Thus, when current is being conducted between two surfaces, it normally travels through the points of contact, meaning that it must become bottlenecked in order to get through. This bottlenecking of current is known as constriction resistance, shown in Figure 1. Since these surfaces are exposed to a variety of environments and working conditions, contamination may appear or become deposited on the surface, adding another resistance through which the current must pass. This contamination is known as film resistance, as shown in Figure 2.

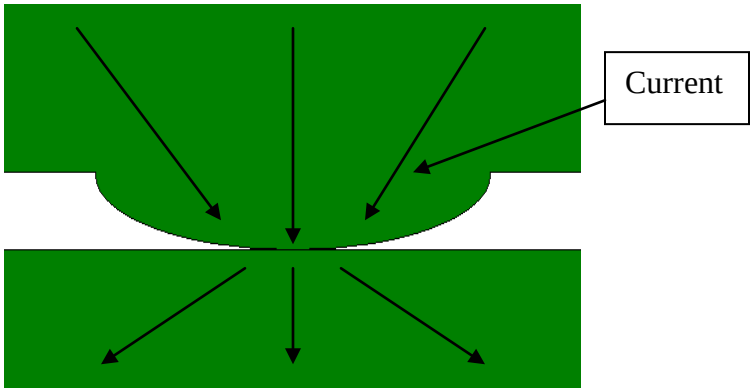

Figure 1 – Picture depicting Constriction Resistance.

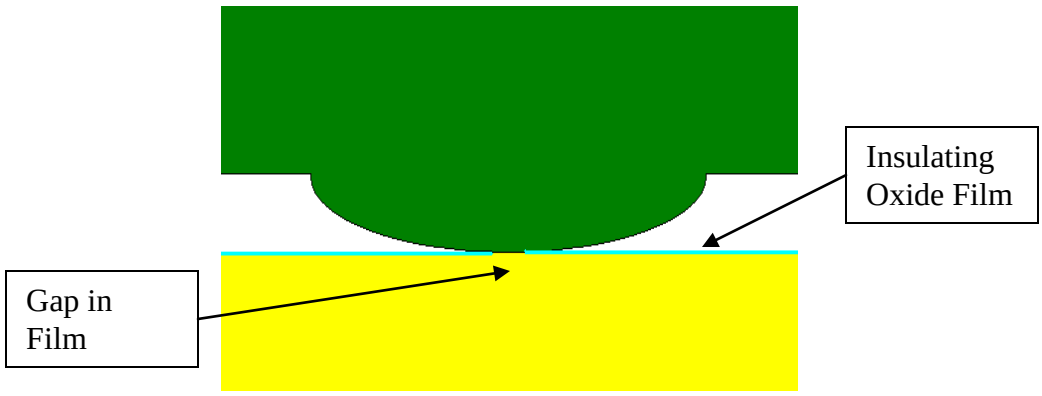

Figure 2 – Picture depicting Film Resistance.

Current rough surface contact models can predict such information as the real area of contact, the average radius of contact, the contact pressure, asperity interference, etc, the mechanical forces acting on the surface and the surface profile. However, none of these models predict what will happen when the surfaces on an electric connector carry current. In Figure 3, the mechanical loads on the surfaces dictate how much of the surface will actually be in contact. This in turn will determine how good the electrical connection between surfaces is. Due primarily to Joule Heating, the morphology of the surface can change, thus changing the mechanical loads acting on the surface, entering the reader into an infinite loop of attempting to calculate mechanical forces, contact area, contact resistance, current field, temperature gradient, mechanical material properties, and back to mechanical forces.

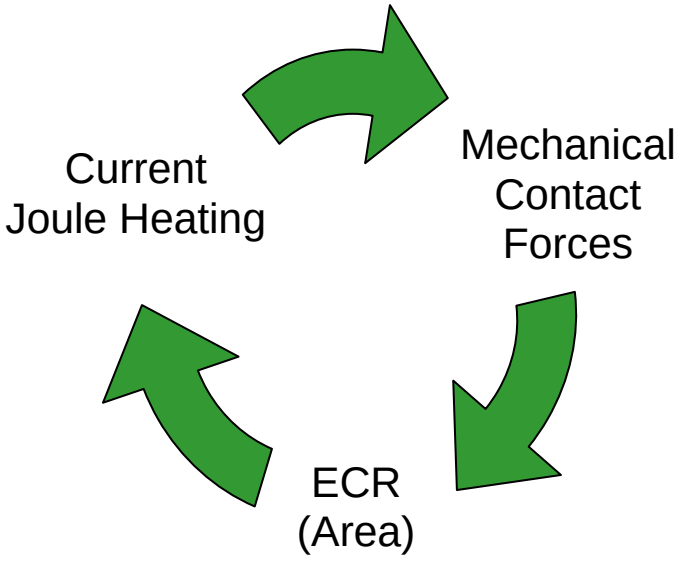

Figure 3 – Depiction of Multi-Physics Dependency Phenomenon.

The mechanical, rough surface contact, electrical, and thermal models must be coupled in order for a comprehensive model to accurately characterize the behavior of an electrical connector. The following equations are the elasticity equations, in cylindrical coordinates, where longitudinal strain is dependent on normal stress, shear stress, and thermal expansion, which depends on the temperature field.

$$\varepsilon_r = \frac{1}{E}\left[\sigma_r - \nu\left(\sigma_\vartheta + \sigma_z\right)\right] + \alpha\Delta T \tag{1}$$

$$\varepsilon_\vartheta = \frac{1}{E}\left[\sigma_\vartheta - \nu\left(\sigma_r + \sigma_z\right)\right] + \alpha\Delta T \tag{2}$$

$$\varepsilon_z = \frac{1}{E}\left[\sigma_z - \nu\left(\sigma_r + \sigma_\vartheta\right)\right] + \alpha\Delta T \tag{3}$$

$$\gamma_{r\vartheta} = \frac{2\left(1+\nu\right)}{E}\tau_{r\vartheta} \tag{4}$$

$$\gamma_{rz} = \frac{2(1+\nu)}{E}\tau_{rz} \tag{5}$$

$$\gamma_{\vartheta z} = \frac{2(1+\nu)}{E}\tau_{\vartheta z} \tag{6}$$

The following is the Electrical Field Equation. Current is dependent on electrical conductivity and the gradient of the electric potential field. Depending on the material, electrical conductivity may be highly dependent on temperature.

$$I = \sigma \nabla \Phi \tag{7}$$

The following is Fourier's Law, where the total heat *Q* includes the effect of Joule Heating. Heat depends on thermal conductivity and the gradient of the temperature field. Again, depending on the material, thermal conductivity may be highly dependent on temperature.

$$Q = k \nabla T \tag{8}$$

The following is the heat contribution due to Joule Heating.

$$Q_{joule} = I^2 \rho \tag{9}$$

As one can see, performing an analysis on an electric connector will turn out to be more complicated than originally anticipated. As of right now, little work has been done utilizing the multi-physics phenomena at play in the connector.

The author completed a survey of current literature on the modeling and testing of electrical connectors to determine exactly how the new research would compliment existing work. This insures that this work is original and recognizes past advancement as applicable, as it relates to electrical connector performance and reliability, and that this work presents data and conclusions that conform well to accepted natural law and theory.

The work available in the public domain generally focuses on two different aspects of electrical connector performance and reliability: the experimental results from performing accelerated tests and the theoretical results from modeling accelerated tests.

2.1 Experimental Case Studies Examining ECR

In examining the literature available on the experimental results, the author has chosen to break this section into three parts: the general behavior of contact resistance, the effects of current through the contact, and the effects of ambient conditions. The material and dynamic considerations, consisting of the materials of the connector and of the displacement amplitude, the vibration frequency, and the contact geometry affecting the connector respectively, are usually included in the accelerated tests.

2.1.1 General Behavior of Electrical Contact Resistance

Holm, in modeling electric connectors, determined the relationship between contact area and contact resistance [14]. In continuing the work on electric connectors, one of the first thorough examinations of electrical contact resistance, ECR, was done at the Research Laboratory for Physics and Chemistry of Solids, Department of Physics, University of Cambridge in the late 1950's. The laboratory released three separate papers with at least J.B.P. Williamson or J.A. Greenwood as primary authors. In Part I of Electrical conduction in solids, Bowden and Williamson investigate the influence of current on the contact between solid [15]. The authors investigated pure gold contacts with a contact geometry of a sphere on a flat. The sphere had a radius of 0.75 mm. The contact interfaces were rigorously cleaned before being subjected to a contact force between 0.01 – 100 grams. No vibration was applied. Current was pulsed, where the authors supplied several different waveforms with different maximum amplitudes. ECR

was measured before and after the pulse or series of pulses. The authors found that no change in ECR occurred unless a critical ECR value was reached, and that the change in ECR did not depend on the shape or duration of the pulsed current. Based on the following equation

$$R_c I_{\max} = C \tag{10}$$

where R_c is the critical contact resistance value, $I_{\max}$ is the maximum current, and C is a constant, the critical contact resistance decreases for increasing $I_{\max}$, which happens due to an increase in the real area of contact at the contact interface. Using the relation between temperature of a contact and the voltage difference across the contact developed by Kohlrausch

$$U^2 = 8\int_0^{\theta} \lambda\rho d\theta \tag{11}$$

where U is the voltage difference across the contact interface, λ is the thermal conductivity, ρ is the resistivity, and θ is the supertemperature, or the temperature of the contact at the interface, the authors discovered that the contacts could collapse, even if the voltage difference across the contact wasn't large enough to push the supertemperature to the melting point. Thus, there seems to be a critical temperature that, when reached at the contact, will result in melting provided the current load is maintained. This melting will result in an increase of the real area of contact and a subsequent decrease in ECR.

In Part II, Greenwood and Williamson developed a theory of temperature-dependent conductors [16]. In developing the theory, it was found that the electric current field can be described solely by the contact geometry and the physical properties

of the medium under certain conditions. They also found that the temperature may be described by the product of the current passing through the contact and the "cold resistance" of the medium. The authors were able to find an upper limit to the product, meaning that there is a maximum current which can flow under steady conditions through a specific geometry of the conductor. A current larger than the maximum will force the temperature to rise until steady state may be reached again.

In Part III, Greenwood and Harris investigated the contact of iron surfaces with contaminating oxide layers [17]. For "clean contacts," the product of final contact resistance R_0 and I remained constant. For "contaminated contacts," the product of final contact resistance R_0 and I increased with the amount of contamination. The product for "clean contacts" was close to the theoretical prediction for iron contacts, however, the value for "contaminated contacts" was 2-3 times higher. The contact geometry was a sphere on flat, where the sphere had a 3.0 mm diameter. The surface was smoothed using 600 grade silicon carbide paper. No vibrations were applied. The authors found that contamination of the contact increases the critical product of the current and the final contact resistance. At equilibrium, contamination has negligible effects. In transient conditions, heating depends on the subareas designated by contamination and not to the contact area as a whole.

From experimental measurements of the resistance of electrical connectors during vibration, several researchers have found three primary phases to the behavior of contact resistance when subjected to fretting motion. In the first phase, the connector exhibits an initially high contact resistance value which then asymptotically decreases to a lower stable value [8],[18]. Contact resistance decreases in the first phase primarily due to the

improvement of the contact as a result of the relative motion and wear between the two contacting surfaces. Both surfaces become relatively smoother, thus enlarging the contact area and lowering contact resistance. Oxides and contaminants may also be removed during this initial phase. In the second phase, contact resistance remains low and stable. The duration of low, stable contact resistance depends on the displacement amplitude and frequency of the fretting motion applied to the connector. In the third phase, contact resistance begins to increase and continues to increase, usually several orders of magnitude beyond the low contact resistance of the second phase. The third phase would usually be considered degradation and the start of eventual failure.

Several papers have explored connectors operating under fretting conditions. Malucci took previously obtained data from other sources in an effort to characterize fretting corrosion and contact instability [7]. All interfaces explored by the author were some form of tin on tin and were only subjected to at most a few thousand cycles of relative motion. Contact and connector geometry differed from source to source, but Malucci was able to come to a few general conclusions. In conducting accelerated tests for connector fretting, he found that oxidation rate, stress relaxation, fretting amplitude, and fretting cycles are useful to consider in the models. Tin plated contacts have a stability contact resistance around 0.05 – 0.1 Ω, beyond which the contacts progress to instability and ultimately fail. van Djik, Rudolphi, and Klaffke investigated connector fretting as it related to the partial slip and gross slip regimes [19]. The authors used a crossed cylinder contact geometry, whose material was a tin bronze dipped in tin, tin intermetallic, tin in heat treatment, and gold and silver with nickel underplating. Contacts were oscillated at 10 Hz for 10,000 cycles with an average normal loading between 2-5

N. The experiment confirmed that a transition from the partial slip to the gross slip regime at 2.5 microns coincided with the transition from stable to unstable electrical behavior, with failure defined as contact resistance greater than 0.5 Ω.

McBride studied the intermittent behavior of electrical contacts for *in-vivo* electrical systems [8]. The author defined intermittent behavior as contact resistance jumping or falling to a high or low level for a period of time and then returning to a stable value. Intermittencies tended to behave similarly to the three phases of behavior for contact resistance, high in the beginning, low in the middle, and high during failure. In a thermally controlled clean room, the author conducted tests using a nickel-cobalt-chromium-molybdenum alloy in a crossed cylinder contact geometry. McBride found that the displacement amplitude has a critical influence on the contact performance and the number of intermittency events.

Rudolphi and Jacobson conducted experiments examining fretting as the mechanical means causing contact degradation in silver coated electrical contacts [20]. They used a crossed cylinder contact geometry that had a copper substrate and silver coating of varying thicknesses. Experiments were conducted at room temperature on dry, un-lubricated samples. Contacts were shaken at 100 Hz with an applied normal force of 10-50 N. Since the contact pairs were subjected to a combination of high normal forces and low displacement amplitudes, most of the contact area tended to become cold welded. Contact resistance tended to exhibit the same behavior as tin contacts previously mentioned by Malucci [7].

In an effort to characterize contact behavior, Jedrzejczyk, Fouvry, and Chalandon also used the transition from partial slip to gross slip as a method to characterizing

fretting [5]. The authors built an apparatus that would simulate the operating environment of a vehicle, including such variables as amplitude displacement, vibration frequency, ambient temperature, and relative humidity. The contact geometry was a crossed cylinder. Contact materials were categorized as noble and non-noble with the noble being gold plating deposited on a nickel interlayer on top of a bronze substrate and the non-noble as non-coated bronze. The displacement amplitude was varied from 0.5 – 40.0 microns, and the vibration frequency was varied from 1 – 500 Hz. The contact normal force was varied from 0.5 – 5.0 N. The relative humidity varied from 1 – 99%, and the ambient temperature varied from 20 - 160°C. Results found that the transition from partial slip to gross slip acts as a threshold for stable and unstable contact behavior.

2.1.2 Effects of Current on ECR

In studying contact degradation, consideration needs to be given to the influence of electrical current and to the environmental effects on contact performance. Bansal and Streator examined the effect of increasing current through an electrical contact [21]. The contact geometry of the experiments was a sphere on a flat with the contact material being aluminum. In the first set of tests, the sphere was brought into contact with the flat, held in place with a normal force of 4.5 N, was powered, and was removed before the next electrical cycling. In the second set of tests, the sphere was brought into contact with the flat, was powered for all currents, and was removed after all electrical cycling had completed. Current, either at low values of 0.01 – 1 A or high values of 1 – 50 A, was maintained for ten seconds, allowing the authors to take an average voltage for the period. Currents started at their lowest value, were then stepped up to their highest value, and then stepped down to their lowest value. In the first series of tests, voltage tended to

saturate quickly for increasing current while contact resistance approached a set value. For decreasing current, both voltage and contact resistance decreased along a different path than the values associated with increasing current. In the second series of tests, contact resistance had different paths for increasing and decreasing currents in the first cycling, but all subsequent cyclings had very similar paths for increasing and decreasing currents. The contact was not subjected to any relative motion during the test. Contact resistance tended to be path dependent based on the morphological changes of the surface, because of material softening or melting, due to the reaching of a critical voltage.

Park, Bapu, and Lee also investigated the influence of increasing current through an electrical contact [10]. The authors also used a sphere on flat contact geometry with the contact material being brass with tin coating. The contact was subjected to a normal load of 0.5 N. The authors subjected the contact to a displacement amplitude of ± 25 microns at a frequency of 3 Hz for 5,100 cycles. The tests were carried out at 25°C at a relative humidity of 45-50%. Current loads were 1,2,and 3 A. The authors found that current loads change the wear debris size and the scarring location. Also, higher current didn't appear to change the failed resistance value, but the number of cycles to failure was inversely proportional to current.

2.1.3 Effects of Materials and Ambient Conditions on ECR

Bruel, Smirou, and Carballeira investigated the gas environments on connector performance [18]. The authors used a crossed cylinders contact geometry and tested the following materials (silver, copper, brass, leaded brass, and nickel). All specimens were preconditioned to the atmosphere (air, argon, nitrogen, sulfur hexafluoride, and 90-10 nitrogen-hydrogen mixture) for 15 hours. Contacts were subjected to a normal load of

0.3 N and moved at a displacement amplitude of 10 microns at 50 Hz. Electrically, the open circuit voltage was limited to 20 mV and the current was limited to 200 μA. From their experiments, the authors found that the time evolution of contact resistance matched well with documented results, that an increase in relative humidity results in a delay of failure, and that non-oxidant atmospheres improve connector reliability.

Park, Narayanan, and Lee examined the effect of ambient temperature on tin-plated copper contacts [9]. The authors used a contact geometry of a sphere on flat with a material of copper covered tin. The contact was subjected to a displacement amplitude of ± 90 microns at a frequency of 10 Hz under a normal load of 0.5 N. The contact was powered at 100 mA. In air at a relative humidity of 45%, ambient temperature was controlled between 25-185 °C. At 85 °C, tin begins to soften, leading to an extended region of contact area and decreasing contact resistance. However, as temperature increased, the presence of Cu-Sn intermetallic compounds began to increase, causing an increase in contact resistance. The study concluded that tin was unsuitable for connector applications at high ambient temperatures because it had a tendency to "wear out," leaving the undesirable intermetallic as the contact material.

2.2 Numerical Modeling of ECR

In examining the literature available on the theoretical results, the author has chosen to break this section into three parts: the use of surface contact models, the use of probabilistic models, and the use of finite element analyses. The use of surface profile models includes the Wilson et al multiscale method [30], but since that is an integral component of this research, it will get its own chapter. The probabilistic model presented offers a unique way to explore connector reliability for connector systems with multiple

contacts. Of greatest interest regarding this research, finite element analyses have been used to predict electrical contact resistance, surface interference, contact pressure, and wear rate.

2.2.1 Rough Surface Contact Models

Ciavarella, Murolo, and Demelio used a fractal description of the surface as a method for predicting constriction resistance in the elastic regime and took experimental results to validate the model [22]. The model shows that as pressure increases, contact resistance asymptotically approaches 0Ω. Using the Archard model applied to the Weierstrass series, the model gives a simple approximate method for computing constriction resistance of a multi-scale surface profile. Findings indicate that the main contribution to the constriction resistance comes from the largest wavelength, suggesting that macroscopic features of the surface dominate.

Gallego and Nelias modeled wear under partial slip and gross slip conditions [23]. As contacts undergo relative motion, friction and adhesion can pull material away from one of the contact surfaces. That material can either remain in the contact region or be ejected from the contact region, thus adding to the film resistance of the contact, an integral part to contact resistance. The model simulates surface wear based on friction energy of the contact. The model does not include the creation and ejection of debris, but it does show that the wear rate decreases with time for both partial slip and gross slip. It also shows that if the friction coefficient remains stable, wear can reinforce the fretting regime in which the contact is operating.

Kogut and Etsion investigated electrical conductivity and friction force in compliant electrical connectors [24]. The contact was modeled as a compliant curved

beam against a rigid flat. The model included such parameters as applied load, surface hardness, surface roughness, and beam geometry. In the end, it was found that surface roughness and surface hardness affect electrical conductivity and friction force. Smoother surfaces result in higher friction forces and higher electrical conductivity. Softer surfaces result in lower friction forces and higher electrical conductivity. Changes in the angular span of the beam do not result in changes in electrical conductivity and friction force.

Jang and Barber analyzed the effect of contact statistics on electrical contact resistance [25]. Working under the assumption that contact does not occur perfectly and at one location, the combined effect of forcing the current through the isolated asperity contacts and clustering of contacts leads to the following contact resistance

$$R = \rho\left(\frac{1}{2Na} + \frac{1}{2\alpha}\right) \tag{12}$$

where N is the number of contact spots and α is the radius of a cluster. The authors show that as finer scales are introduced, the predicted resistance approaches the perfect contact limit, denoted in the following equation.

$$R = \frac{\rho}{2a} \tag{13}$$

where ρ is electrical resistivity and a is the radius of contact.

2.2.2 Probabilistic Models

Most connectors don't have a single point of contact but many points of contacts. Swingler and McBride investigated the reliability of these multi-contact connectors [11]. The authors studied several sets of commercially available connectors with multiple contacts. All test samples were given a displacement amplitude of 80 microns at 3 mHz.

The model rests on several assumptions. First, failure for a contact, experimentally, occurs at 200 mΩ, which is arbitrarily chosen. Second, for a connector in the model to have failed, all contacts in the connector must have failed at the same time. Third, the probability density function for determining if a contact has failed is based on a Weibull distribution. Fourth, the model assumes a constant normal contact force, which may not be true. The authors found that this probabilistic model for connector reliability shows an exponential improvement in reliability with an increasing number of contact interfaces.

2.2.3 Finite Element Analyses

Researchers have regularly used finite element software to model contact. However, some researchers have used other methods. For example, Tristani, Zindine, Boyer, and Klimek attempted to model an electrical connector mechanically using springs [12]. The authors sought to determine the evolution of the tangential force, causing relative motion, versus displacement. The experiments used a blade and receptacle electrical connector, made from a tin-plated copper alloy. The female end had a stiffness of about 0.015 N/micron. The connector was subjected to a displacement amplitude of 50 microns at 10 Hz. The resulting tangential force versus displacement plot resembled a trapezoid. The authors found that the best mechanical to fit this tangential force versus displacement plot was a longitudinal spring connected to a vertical spring situated in a wear scar. The resulting force versus displacement curves for a given number of cycles matched well with the experimental results, depending on the initial profile. The spring models did not include any non-linearities, such as plastic deformation or fatigue.

Noyes and Green examined the effect of conductive fluids surrounding asperity contact [26]. The analysis focuses on a sphere on sphere contact geometry with the contact materials being aluminum and copper. The authors use multi-physics finite element analysis, imparting low interferences to insure only elastic deformation occurs, to predict contact force, pressure, and area of contact. Surrounding the asperity is either air, of low electrical conductivity, or liquid gallium, of high electrical conductivity. They concluded that at low voltages across the contact, the magnetic forces in the fluid do not have an effect on the contact force and that there exists an inverse relationship between fluid conductivity and current density through the contact.

Lee, Cho, and Jang demonstrated a working FEA of multiscale contact that showed that contact resistance approaches a finite value for increasing the number of scales of a surface [6]. The model assumes that points of contact will be clustered and not randomly distributed across the contact surface. Using the random midpoint displacement algorithm, the authors generate an arbitrarily rough surface modeled by finite elements. Contact resistance is then gathered from the simulation, which corresponds well to Greenwood's model [27].

In an effort to model some of the complexities associated with contact, McColl, Ding, and Leen developed an FEA tool for simulating fretting wear and the evolution of fretting variables for a cylinder on flat configuration [28]. The wear equation is based on Archard's equations and implemented within the finite element package. Given these values, the application can then predict the relative change in geometry and change in fretting wear variables (relative slip, contact pressure, and sub-surface stresses). The simulation is run externally from the FEA in the following order: initialize parameters,

generate finite element model, calculate contact pressure and slip distribution, calculate nodal wear using Archard's equation, if at end of cycles, quit; else, update nodal coordinates and revise finite element model. The simulation results are compared to experimental results for a cylinder on a flat undergoing a displacement amplitude of 50 microns at a frequency of 20 Hz. The wear scar profiles generated by the fretting test and the finite element model correlate well, with the simulations usually under-predicting the depth of the profile. In the case of low normal loading, the profiles match well. As a corollary to this research, Ding, McColl, Leen, and Shipway simulated the effect of debris on fretting wear [29]. Wear debris modeled as an anisotropic elastic-plastic layer structure in the finite element analysis, where the model determines contact pressure and slip distributions as before and the simulation calculates the amount of nodal wear using the Archard equation. With some experimental results, wear scarring and depth are accurate within about 25% of experimental results.

Since most electrical connectors have plating on a substrate, Ossart, Noel, Correia, and Gendre modeled them using a finite element analysis [30]. The finite element model simulates a sphere on a flat, with tin plating on both surfaces and brass as the substrate. A multi-physics analysis was performed to compute contact resistance and determine the geometry of the contact using an elastic-plastic model. Calculated values from the simulation are the same order of magnitude as experimentally obtained values.

Abdi, Beloufa, and Benjemaa explored the changes in resistance for different loadings and contact geometries and validated these experimental results using FEA software [2]. The contact geometry was a sphere on a flat with the contact material being copper alloy. In the first set of tests, contact resistance was measured for an applied

current equal to 10 A while normal contact force was increased from 1 – 100 N. In the second set of tests, a normal force was applied to the contact after which a tangential force was applied, displacing the contact 1 mm. Tangential forces were 2, 4, 8, 16, 32, 64, and 100 N. The FEM exploited the symmetry of the geometry and only modeled one section of the sphere and flat. The FEM also included surface roughness data obtained from a laser profilometer. Using a logarithmic transformation of the experimental data, the authors used a power law relationship to fit the FEM results. They found that a good correlation between experimental and numerical results occurred for low indentation forces. The contribution due to roughness became negligible as indentation force increased. However, numerical results for the tangential displacement tests did not correlate well as contact resistance became dominated by wear debris, which the model did not include.

CHAPTER 3

Round Pin, High Power Connector Experiment

An experiment was designed and implemented as a way to test the performance and reliability of the high power connectors and the validity and accuracy of the multi-physics model. The connector system, (Figure 4) , consists of three parts: the male end (Figure 5), the female end (Figure 6), and the spring (Figure 7).

Figure 4 – Connector System.

Figure 5 – Male End of Round Pin, High Power Connector.

Figure 6 – Female End of Round Pin, High Power Connector.

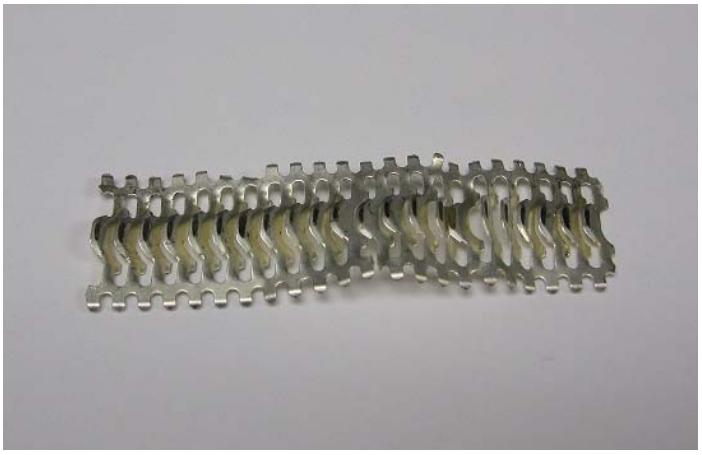

Figure 7 – Connector Spring in Round Pin, High Power Connector.

The spring sits in a groove on the inside of the female end of the connector between the female and the male end of the connector, as shown in Figure 8. The tabs on the spring provide a contact pressure normal to the surface of the male and female end. This contact pressure keeps the spring in contact with the other parts of the connector, thus providing an electrical connection between the male and female ends of the connector.

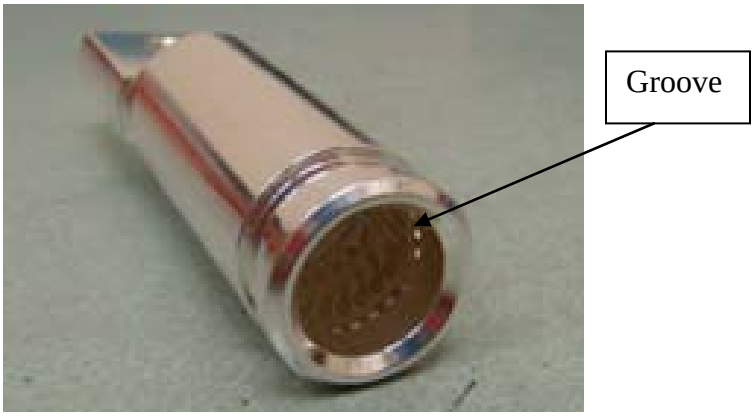

Figure 8 – Connector Spring inside Female End of Round Pin, High Power Connector.

3.1 Test Setup

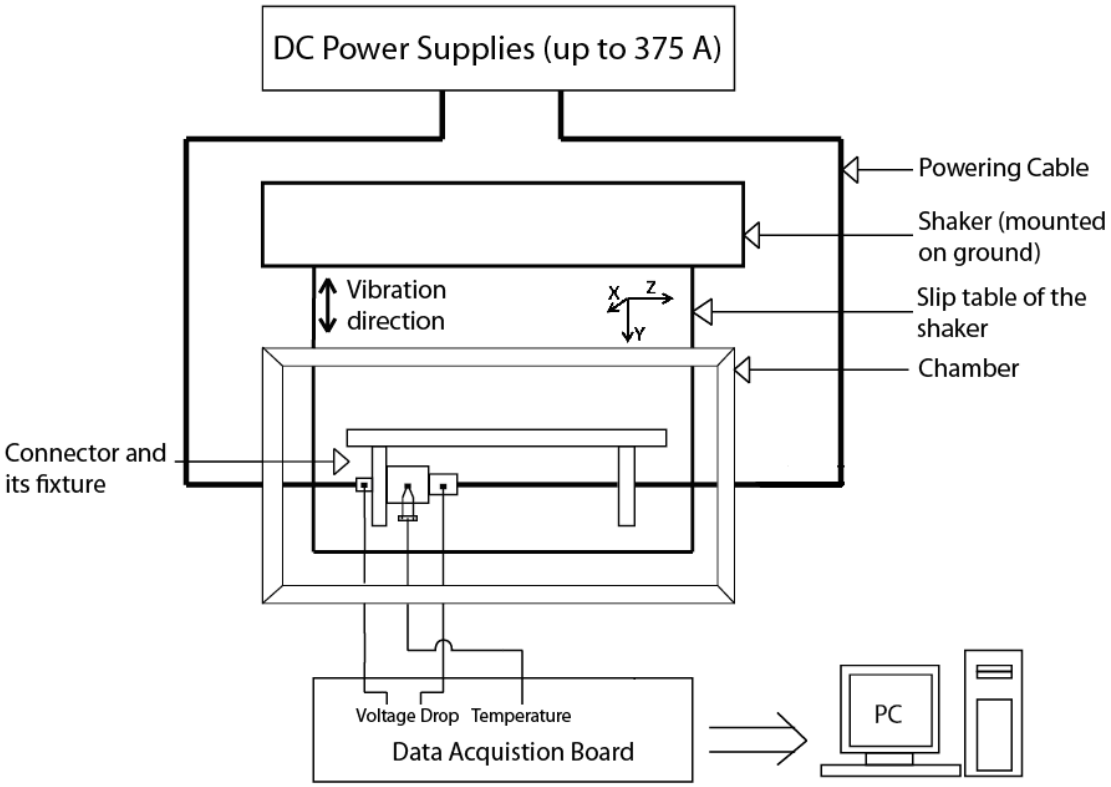

Figure 9 – Layout of Connector Experiment and Measuring Devices.

Figure 9 shows the layout of the connector experiment. Current is applied to the connector by three Sorensen™ DCS-125E power supplies. Unit capacity maxes out at 125A, so multiple units are paralleled together to give the necessary current loading. Temperature is measured by a K-type thermocouple. Electrical contact resistance is measured by a Agilent™ 34411A multi-meter. Measurements from each of these devices are sent to National Instrument™ signal conditioning modules installed in the data acquisition board. Data is then sent to a computer work station for further processing and analysis.

Figure 10 – Connector with bubble wrap and insulating foam.

Power is supplied to the connector via the cable connected to the male end of the connector and to the cable connected to the female end of the connector. In an effort to thermally isolate the high power connector, a packaging bubble wrap was wrapped around the connector. Another layer of insulating foam, designed for hot water pipes, was wrapped around the bubble wrap (Figure 10) . This was done to mimic zero heat

transfer via convection and radiation from the surface of the connector to the surroundings. There is also some heat generated by the cable, due to Joule heating, and depending on the temperature gradient, heat may or may not be conducted to or from the connector by the cable. This heat is impossible to thermally isolate without electrically breaking the connection across the connector.

Figure 11 – Placement of the Thermocouples on Connector for the Experiment.

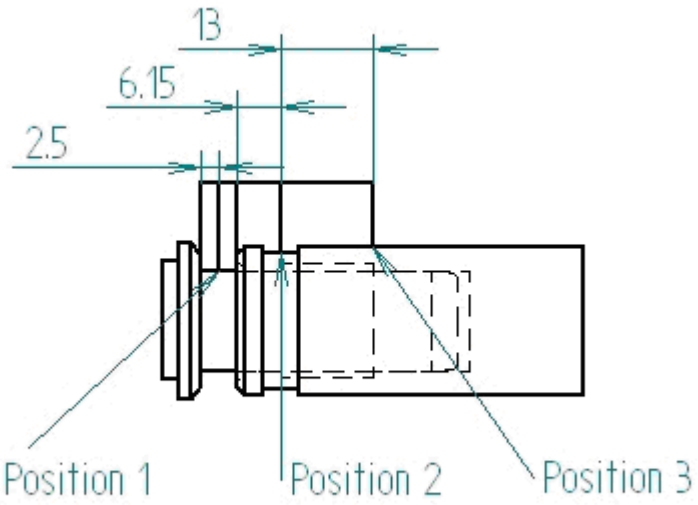

Figure 12 – Schematic Showing Placement of the Thermocouples (mm).

Thermocouples were placed at three separate locations, two on the female end of the connector and one on the male end of the connector, as shown in Figure 11 and Figure 12. The thermocouple placed on the male end of the connector was located 2.5 mm from the edge of the female end of the connector when the two ends were connected. The second thermocouple was located 6.15 mm from the edge on the female end closest to the male end of the connector. The third thermocouple was located 13 mm from the second thermocouple. All thermocouples were placed on the outside surface of the connector.

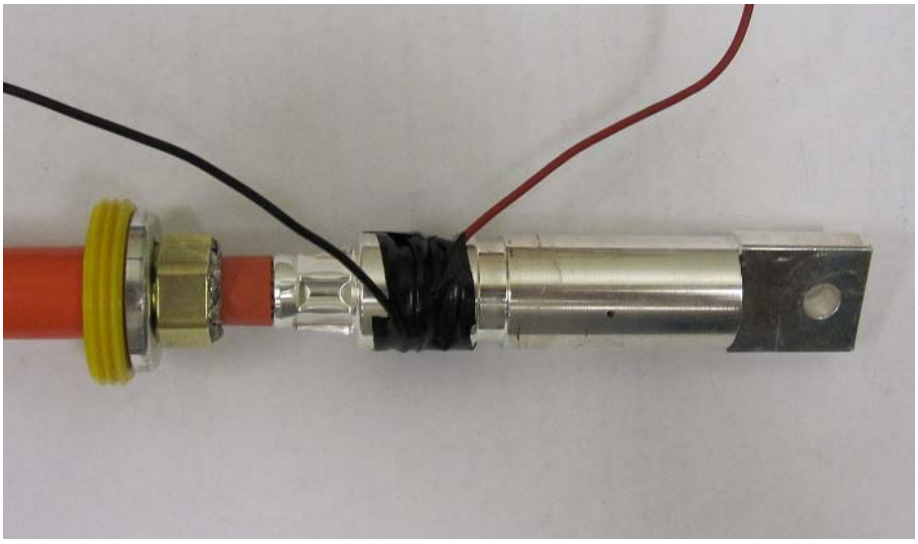

Figure 13 – Placement of the Electrical Leads on Connector for the Experiment.

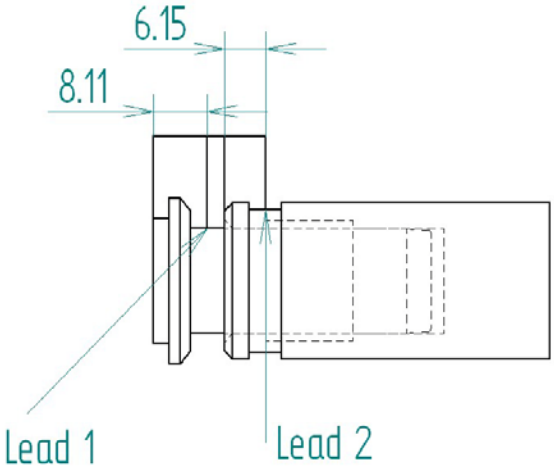

Figure 14 – Schematic Showing Placement of the Electrical Leads (mm).

Electrical leads were placed at two separate locations, one on the female end of the connector and one on the male end of the connector, as shown in Figure 13 and

Figure 14. One of the leads was placed on the male end of the connector was located in the middle of the groove on the male end, just over 8mm from the middle of the gap between the male and female ends. The other lead was placed in the middle of the outer groove of the female end. This placement attempts to utilize the available space on the connector while minimizing effects of bulk resistance. All leads were placed on the outside surface of the connector.

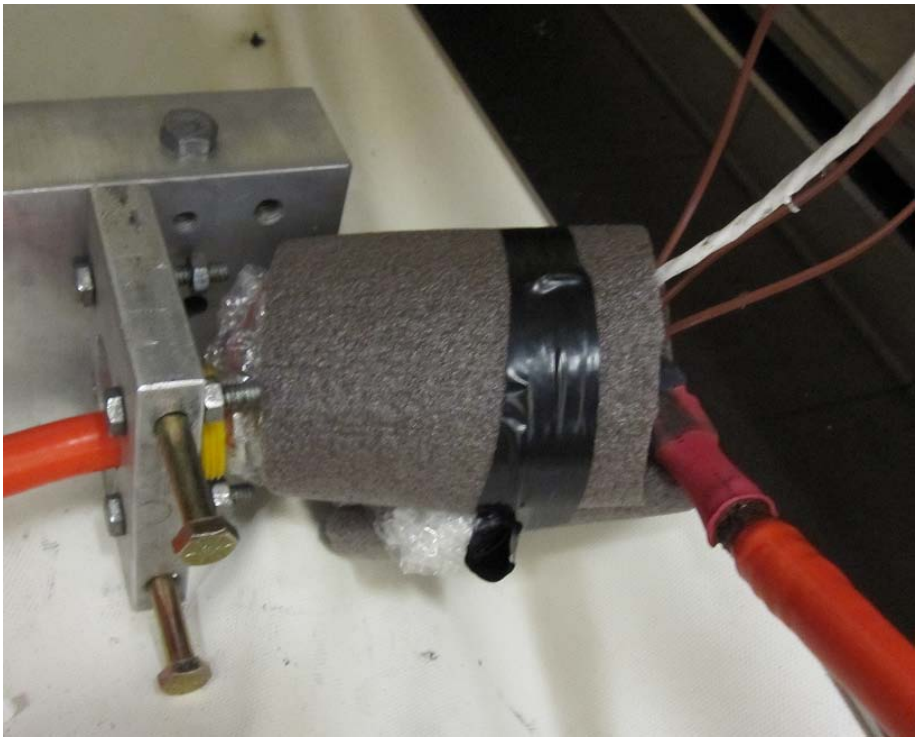

Figure 15 – Setup of High Power Connector on Shaker Table.

Figure 15 shows pictures of the experimental setup used in the lab. The connector is attached to the shaker table using a custom built apparatus, machined and built at the Design and Manufacturing Lab at Auburn University by an undergraduate student. Since

the shaker is not in use for determining the validity and accuracy of the 3-D multi-physics FEA, its dimensions and material are irrelevant here.

3.2 Test Conditions

No vibrations were administered via the shaker table. Relative humidity could be assumed to be between 0-50% based on weather information available for the day the test was conducted. It is assumed that humidity doesn't factor into this test because of its negligible effects on connectors with silver finishes [18]. Ambient temperature in the lab held steady around 25°. Ambient temperature would only have an effect on the amount of heat being conducted to or from the connector based on the temperature of the power cable since the connector, wrapped in two layers of insulation, is thermally isolated from the air in the room and the surroundings of the thermal chamber.

3.3 Test Matrix

The test matrix was governed by powering the connector to a pre-determined amperage and allowing the connector temperature at the thermocouple locations to stabilize. Electrical contact resistances stabilized much more quickly than the temperatures. Current loading began at 25A and increased by 25A increments to 225A.

3.4 Test Results

Below are the results for the connector experiment in Table 1. These results are for the stabilized temperature results from the thermocouples. All temperature results are measured in °C, and all electrical contact resistances are measured in mΩ. Figure 16 shows the increasing trend of ECR with respect to increasing current. Figure 17, Figure 18, and Figure 19 show the increasing trends of temperature with respect to increasing current. This is to be expected as the connector is subjected to Joule heating, and very

little heat should escape due to the presence of the insulating foam wrapping, thus resulting in an increase in temperature on the surface of the connector.

Table 1 – Stabilized Experimental Results of Temperature and ECR

Current	T1	T2	T3	ECR
25A	25.721	25.718	25.719	.023693
50A	29.058	28.96	28.857	.025434
75A	34.424	34.209	33.928	.026274
100A	41.332	40.882	40.322	.026841
125A	50.399	49.665	48.687	.02742
150A	61.045	59.964	58.439	.027962
175A	74.151	72.481	70.299	.028278
200A	91.47	88.91	85.929	.028513
225A	104.85	101.93	100.01	.028871

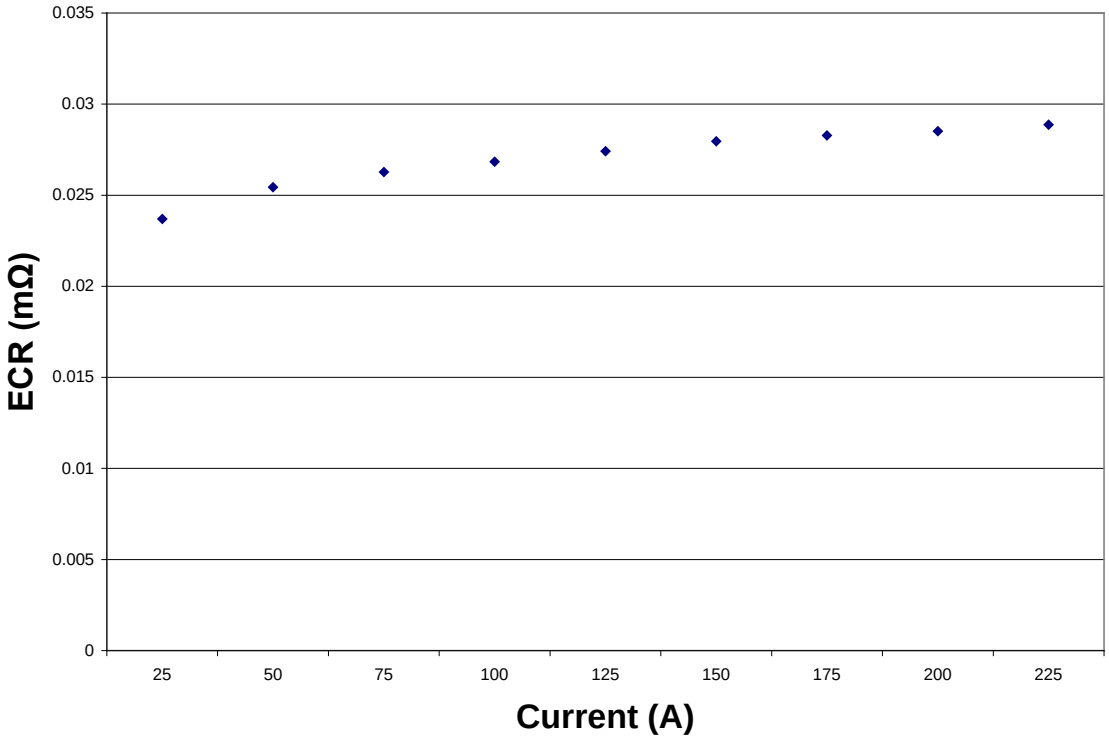

Figure 16 – Experimental ECR vs. Current.

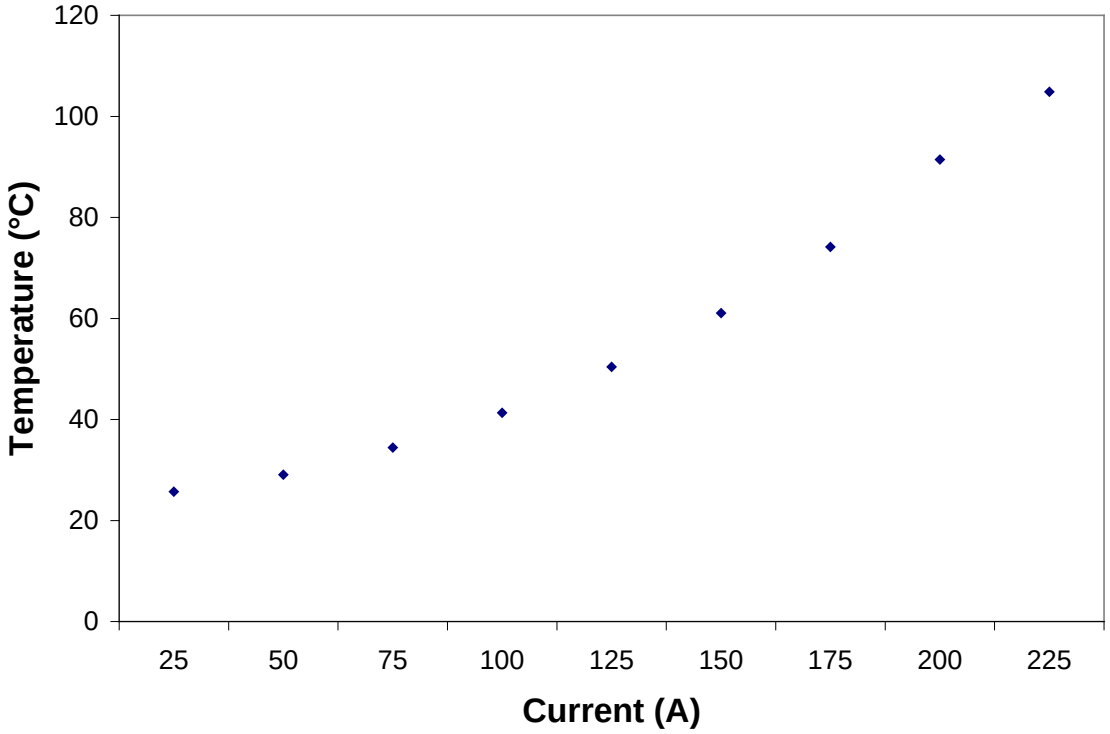

Figure 17 –Temperature at Position 1 vs. Current.

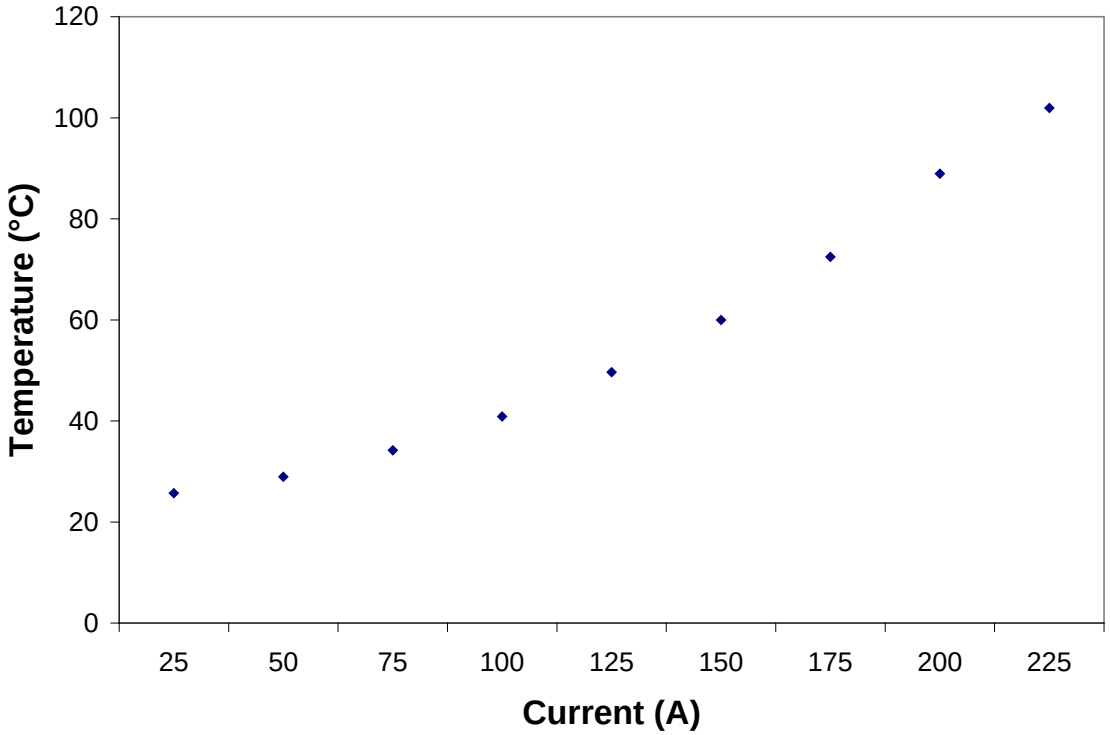

Figure 18 –Temperature at Position 2 vs. Current.

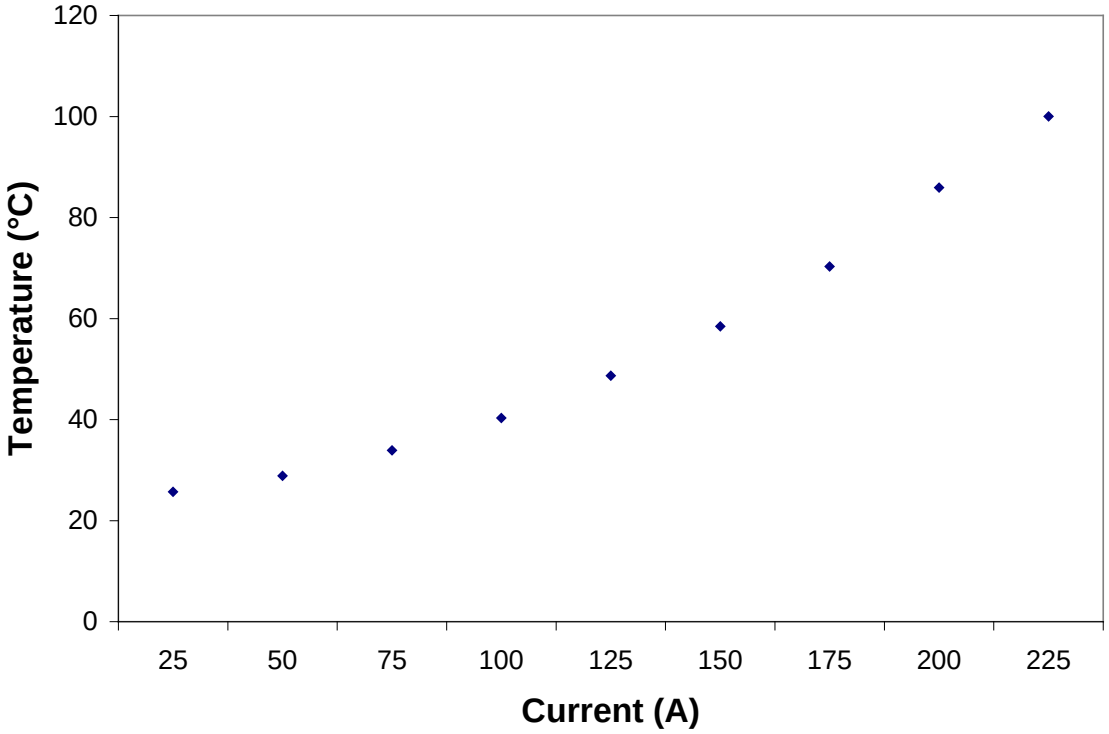

Figure 19 –Temperature at Position 3 vs. Current.

CHAPTER 4

Multi-Scale Modeling of Electrical Contact Resistance

As shown in the introduction, little work has been done on the modeling of high power connectors. Most of the experimental work available attempts to keep voltages and amperages low to avoid thermally induced surface degradation. Even less work has been performed using multi-physics technologies, i.e. solving the coupled electrical, thermal, and mechanical field equations. Of the work that has been done using multi-physics technologies, little to none has incorporated multiscale surface properties.

4.1 Multi-Scale Methodology

Even though they may appear smooth, all engineering surfaces are rough at some scale. Modeling rough surfaces can be done using statistical [27, 31, 32], fractal [33, 34], or multiscale methods [35, 36]. This research uses the Wilson et al. multiscale methodology [13] for computing electrical contact resistance. The output from the multiscale methodology is electrical contact resistance as a function of contact pressure. First, a surface is measured using a profilometer. A fast Fourier transform is taken of the surface profile. The area of contact and average radius of contact at each scale is then calculated. For the perfectly elastic case, the following equations are used to determine area of contact at each scale.

Equations 13-15 are from John, Greenwood, and Higginson [37].

$$\left(A_{JGH}\right)_1 = \frac{2\pi}{f^2}\left[\frac{3}{8\pi}\frac{\bar{p}}{p^*}\right]^{2/3} \tag{14}$$

$$\left(A_{JGH}\right)_2 = \frac{1}{f^2}\left[1-\frac{3}{2\pi}\left[1-\frac{\bar{p}}{p^*}\right]\right] \tag{15}$$

$$p^* = \sqrt{2}\pi E' \Delta f \tag{16}$$

Equations 16-17 are from Jackson and Streator [36].

For $\frac{\overline{p}}{p^*} < 0.8$

$$A = \left(A_{JGH}\right)_1 \left(1 - \left[\frac{\overline{p}}{p^*}\right]^{1.51}\right) + \left(A_{JGH}\right)_2 \left(\frac{\overline{p}}{p^*}\right)^{1.04} \tag{17}$$

For $\frac{\overline{p}}{p^*} \geq 0.8$

$$A = \left(A_{JGH}\right)_2 \tag{18}$$

For the elastic plastic case, the following equations can be used. Equations 18-22 are from Krithivasan and Jackson [38] and Jackson, Krithivasan, and Wilson [39].

$$A_c = \frac{2}{\pi}\left(\frac{C * S_y}{8\Delta f^2 E'}\right)^2 \tag{19}$$

$$\overline{p}_c = 2A_c p_c f^2 = \frac{1}{24\pi}\frac{\left(C * S_y\right)^3}{\left(\Delta f E'\right)^2} \tag{20}$$

where $C = 1.295 \cdot \exp(0.736\nu)$.

$$A_p = 2\left(A_c\right)^{\frac{1}{1+d}}\left(\frac{3\overline{p}}{4C * S_y}\lambda^2\right)^{\frac{1}{1+d}} \tag{21}$$

$$d = 3.8 \cdot \left(\frac{E'}{S_y}\frac{\Delta}{\lambda}\right)^{0.11} \tag{22}$$

$$\frac{p_{ep}^*}{p^*} = \left(\frac{11}{4\left(\Delta / \Delta_c\right) + 7}\right)^{3/5} \tag{23}$$

$$A = (A_P)\left(1 - \left[\frac{\overline{p}}{p_{ep}^{*}}\right]^{1.51}\right) + (A_{JGH})_2\left(\frac{\overline{p}}{p_{ep}^{*}}\right)^{1.04} \tag{24}$$

The area calculated for both the elastic and elastic plastic above is for one frequency scale only. The total area in contact and total load must be computed for all scales included in the analysis. They are given by the following equations. The subscript *i* denotes the spatial frequency being used.

$$A = \left(\prod_{i=1}^{i_{\max}} \overline{A}_i \eta_i\right) A_n \tag{25}$$

$$P = \overline{P}_i \eta_i A_{i-1} \tag{26}$$

In order to find the average radius of contact per frequency level *i*, the following equation is used.

$$a_i = \sqrt{\frac{A_i}{2 \cdot \pi \cdot A_{i-1} \cdot f^2}} \tag{27}$$

$$\Psi_i = \left(1 - \sqrt{A_i / A_{i-1}}\right)^{1.5} \tag{28}$$

where Ψ_i is the alleviation factor.

The total ECR for the entire surface in contact is then given by the following.

$$ECR_{total} = \sum_{i=1}^{i_{\max}} \frac{\Psi_i ECR_i}{\eta_i A_{i-1}} \tag{29}$$

4.2 Surface Profiles of a Round Pin, High Power Connector

The surface profiles of three different connectors are plotted below using Matlab™. Of the three connectors used, one had not been powered or vibrated, another connector had been powered and vibrated, but not to the point of failure, and the last

connector had been powered to the point of failure. In another project using the round pin high power connector, failure was defined as electrical contact resistance reaching a critical value. The surface profiles were measured using a Veeco Dektak 150 Stylus Surface Profilometer, which has a vertical measurement resolution down to less than a nanometer. The surface profile measurements were taken on the male end of the connector due to the access to the surface.

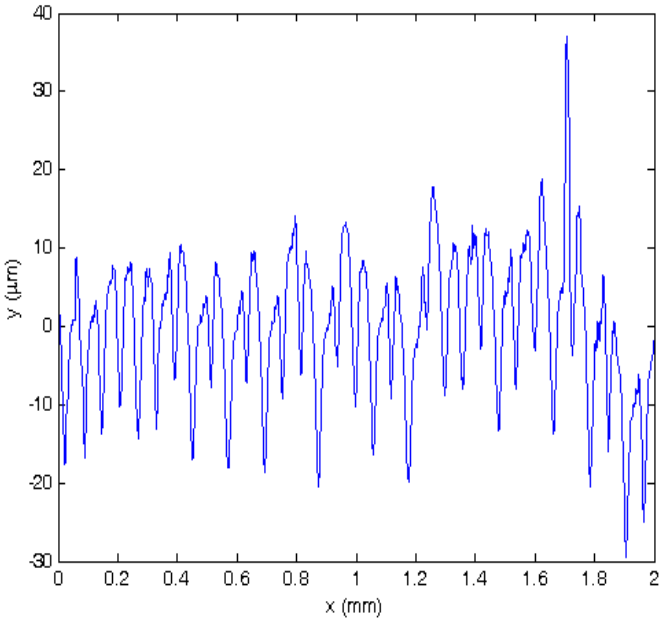

Figure 20 – Surface Profile Measurement 1 of Round Pin, High Power Connector with no wear.

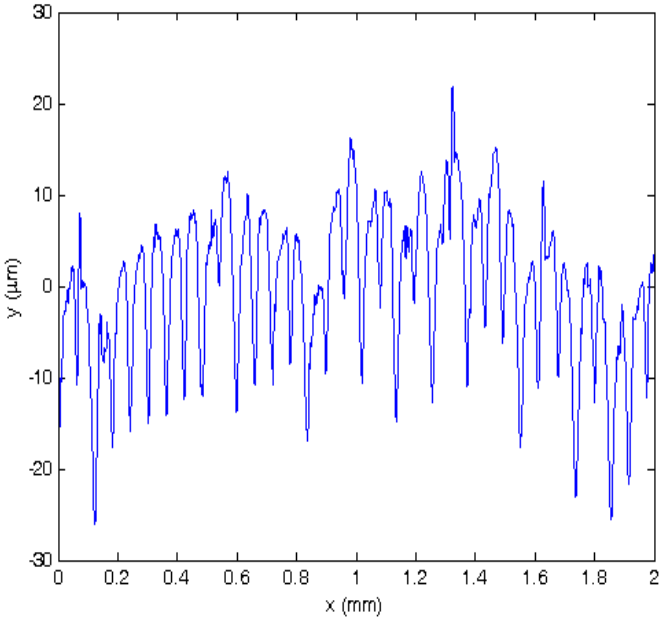

Figure 21 – Surface Profile Measurement 2 of Round Pin, High Power Connector with no wear.

Figure 20 and Figure 21 both show the leveled surface profiles recorded using the stylus profilometer. The connector at the time the surface profile was recorded had not been powered or vibrated yet. The two figures above show the surface profile for the same connector but at different locations on the connector. The amplitude of the surface does not vary much, and the surface appears to exhibit some periodicity, probably due to the machining.

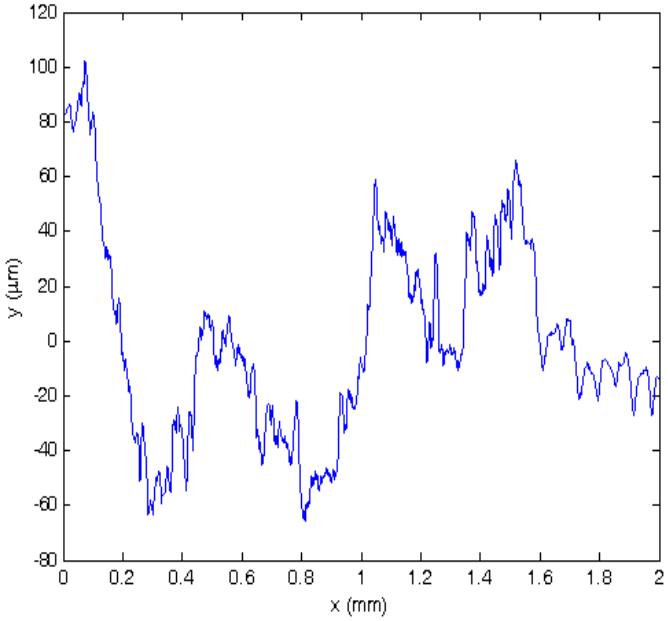

Figure 22 – Surface Profile Measurement 3 of Round Pin, High Power Connector with low wear.

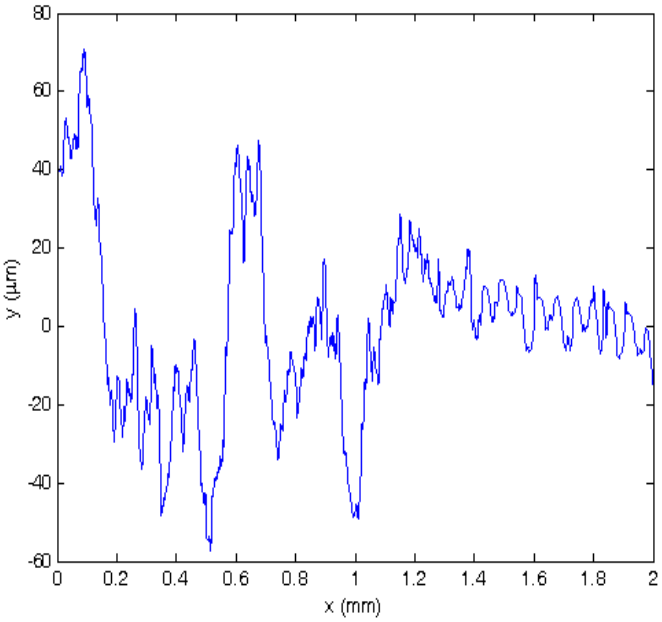

Figure 23 – Surface Profile Measurement 4 of Round Pin, High Power Connector with low wear.

Figure 22 and Figure 23 both show the surface profiles of a worn connector recorded using the stylus profilometer. The connector at the time the surface profile was recorded had been powered and vibrated. The two figures above show the surface profile for the same connector but at different locations on the connector. In Figure 22, a wear scar has appeared between x = 0-1.6 mm. Outside of the scar, the surface appears to have the same periodic profile as shown in Figure 1 and Figure 2. In Figure 23, the wear scar does not appear to be as pronounced as in Figure 3, but two wear scars have appeared between 0.1-0.5 mm and 0.7-1.1 mm.

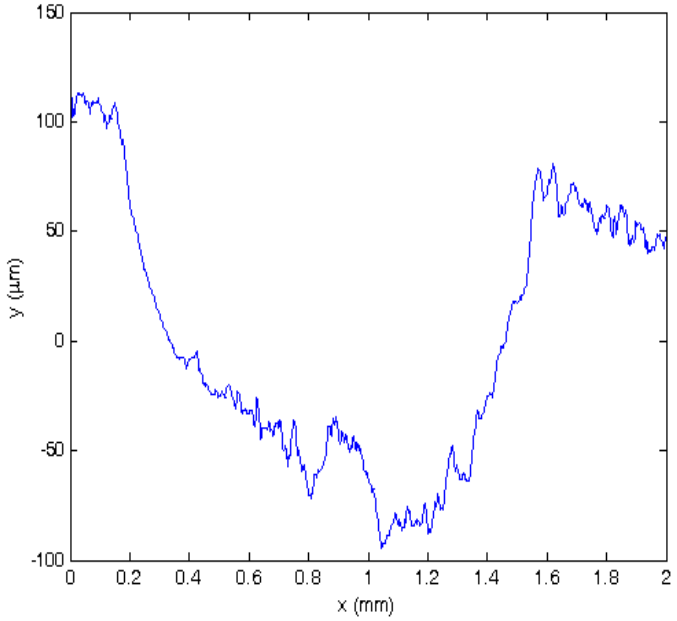

Figure 24 – Surface Profile Measurement 4 of Round Pin, High Power Connector with high wear.

Figure 24 shows the surface profile from a severely worn connector recorded using the stylus profilometer. The connector at the time the surface profile was recorded

had been powered and vibrated. In Figure 24, a pronounced wear scar has appeared between 0.2-1.6 mm. Outside of the scar, the surface appears to have the same smooth profile as shown in Figure 20 and Figure 21. This wear scar also appears to have the most material removed from the surface.

Roughness values were computed for each of the surface profile curves using the equations below. The results of the calculations are in Table 1. All roughness values are in μm. Surfaces 1 and 2 have not been powered or vibrated.

$$R_a = \frac{1}{L}\int_0^L |z| dx \tag{30}$$

$$R_q = \sqrt{\frac{1}{L}\int_0^L z^2 dx} \tag{31}$$

Table 2 – Roughness Measurements from Three Connector Surfaces

Surface	R_a (μm)	R_q (μm)
1	6.8907	8.8271
2	6.551	8.2163
3	28.462	36.018
4	17.045	23.113
5	52.8	59.306

The roughness parameters increase from about 7 μm for the new connector, to 20 μm for a used connector, and to 55 μm for a failed connector. This is nearly an order of magnitude increase in the roughness. While R_a and R_q are adequate values to describe the surface, they inaccurately characterize the surface. Statistical methods do not take into account the different scales of asperities and their respective amplitudes. They also

neglect the lateral distribution of asperities. Using the Wilson et al. multiscale method should remove these problems.

4.3 Multi-Scale ECR of Smooth, Slightly Worn, and Failed Connectors

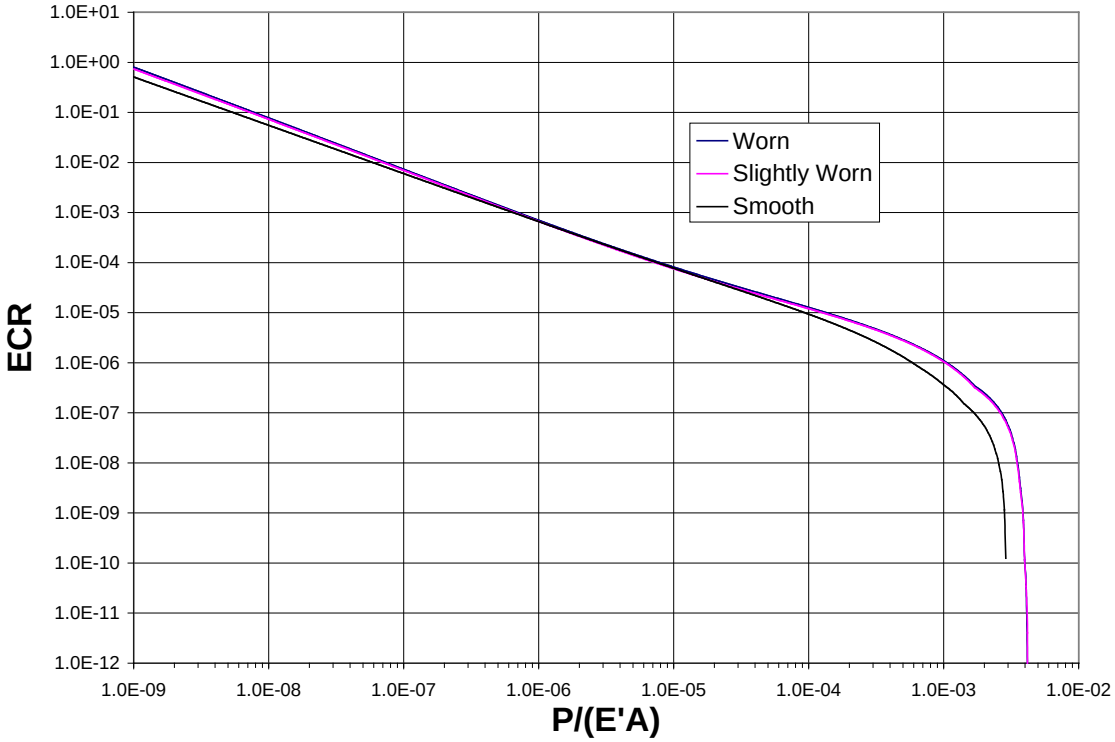

Figure 25 – Contact Pressure vs. ECR for 3 Separate Surfaces (black – smooth, pink – slightly worn, and blue – worn).

Figure 25 shows a plot of predicted ECR as a function of contact pressurefor three separate surface types using the multiscale model. The multiscale model incorporates the material properties of silver, shown in Table 3. The three surface types are from the smooth, slightly worn, and failed surfaces on a round pin connector. ECR for the worn and slightly worn both follow a very similar path. The smooth surface has the lowest ECR at both low normalized contact pressures and high normalized contact pressures. At

intermediate contact pressures, all three surfaces appear to have the same ECR. For all three surfaces, ECR decreases as contact pressure increases.

Table 3 – Material Properties for Silver.

Material Property	Numerical Value
Young's Modulus (E)	76 GPa
Poisson's Ratio (ν)	0.37
Resistivity (ρ)	$1.55\times10^{-6}\,\Omega m$
Thermal Conductivity (k)	419 W/m/K
Coefficient of Thermal Expansion (α)	$19.8\times10^{-6}\,\frac{1}{°C}$

CHAPTER 5

Setup of 2-D Multi-physics FEA

Every finite element analysis tries to balance the physical accuracy of the model with the computational resources needed to perform the analysis. An overly simplified model may only take seconds to solve but could be physically inaccurate. The converse holds, where an elaborately detailed model may give a numerically accurate approximation to the solution but may take an unacceptable amount of time to compute. These competing paradigms led the author to construct two separate ways of solving the connector problem, a 2-D and 3-D method. A 2-D method was tried first, with hopes that the computational efficiency relative to performing a complete 3-D analysis would outweigh any shortcomings.

5.1 Simplification to 2-D FEA Geometry

The connector system, as shown in Figure 4, is composed of three separate parts. There is the male end of the connector (Figure 5), the female end of the connector (Figure 6), and the spring that connects male and female together (Figure 7).

The spring sits in a groove on the inside of the female end of the connector between the female and the male end of the connector, as shown in Figure 8. The tabs on the spring provide a contact pressure normal to the surface of the male and female end. This contact pressure keeps the spring in contact with the other parts of the connector, thus providing an electrical connection between the male and female ends of the connector.

In an attempt to simplify the model, and the corresponding computational effort, the model exploits the connector's various forms of symmetry. The first form of

symmetry encountered is about the shared longitudinal axis of the male and the female ends of the connector. In simplifying the connector for modeling, it should be clear that the male and female ends can be described by a profile, resulting in a cross sectional area, that when swept 180° about the axis of symmetry yields the volume of two of the connector parts. The spring has periodic features, two smaller tabs connecting the spring to the female end of the connector and one larger tab connector the spring to the male end of the connector, but for different angles rotated about the axis of symmetry, different profiles appear. In reality, certain profiles may appear which are not in contact with either the male end or the female end of the connector. Instead of modeling the connector for any profile which may appear, a composite profile, and hence composite mass, may suffice as a possible substitute. Finally, the profile consisting of the male end, female end, and the composite spring may be cut in half as the profiles are symmetric about the line of the axis of symmetry.

5.2 Material Properties

The round pin, high power connector is comprised of three separate parts: the male end, the female end, and the connector spring. All three parts are made of the same materials, an annealed copper with a silver plating finish. The material properties for the annealed copper are listed in Table 4. The material properties for the composite mass representing the spring are listed in Table 5. The material properties for the composite mass are a very crude estimate of what the properties might be. They were added as a way to test the operating capacity of the 2-D multi-physics FEA.

Table 4 – Material Properties for Annealed Copper

Material Property	Numerical Value
Young's Modulus (E)	110 GPa
Poisson's Ratio (ν)	0.343
Resistivity (ρ)	$1.7\times10^{-6}\,\Omega m$
Thermal Conductivity (k)	386 W/m/K
Coefficient of Thermal Expansion (α)	$17\times10^{-6}\,\frac{1}{°C}$

Table 5 – Material Properties for Composite Mass Representing the Spring

Material Property	Numerical Value
Young's Modulus (E)	101 GPa
Poisson's Ratio (ν)	0.37
Resistivity (ρ)	$1.55\times10^{-6}\,\Omega m$
Thermal Conductivity (k)	60 W/m/K
Coefficient of Thermal Expansion (α)	$17\times10^{-6}\,\frac{1}{°C}$

5.3 Elements in 2-D Multi-physics FEA

There is a coordinate axis at the lower left hand edge of every figure below (Figure 26 -). The *x*-direction follows the axis of symmetry along the model and the *y*-direction follows the vertical, or radial, direction. The model is composed of two element types, Plane223 and Link68. Plane223 elements are multi-physics 2-D solid elements with 8 nodes which allow for a coupled structural, thermal, and electrical analysis. Link68 elements are uniaxial 3-D lines with the ability to conduct heat and electricity. After meshing, the system contains 1,516 Plane223 elements and 154 Link68 elements.

5.4 Boundary Conditions in 2-D Multi-physics FEA

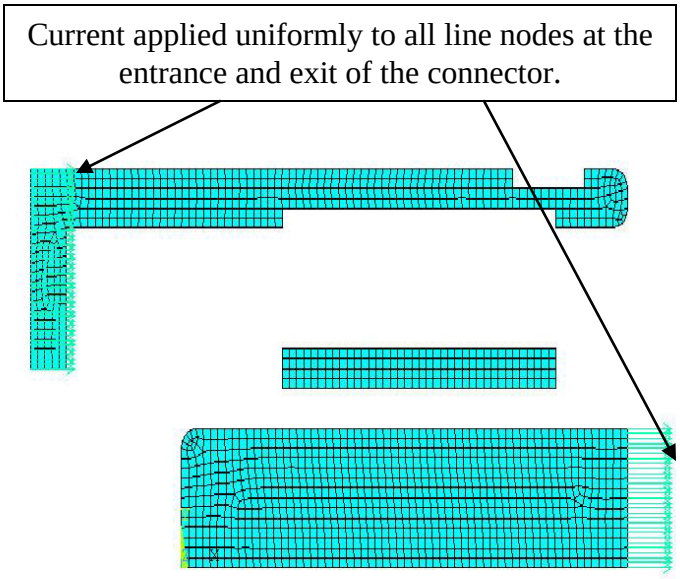

Figure 26 – Current Boundary Conditions for 2-D Multi-physics FEA.

The connector is powered with the appropriate amount of uniform current as shown in Figure 26. Current is applied to each node on either end of the male or female connector. This is done by setting the boundary condition on the lines of the male end and female end of the connector. The current then traveling through the profile of the connector is half of the total current traveling through the connector.

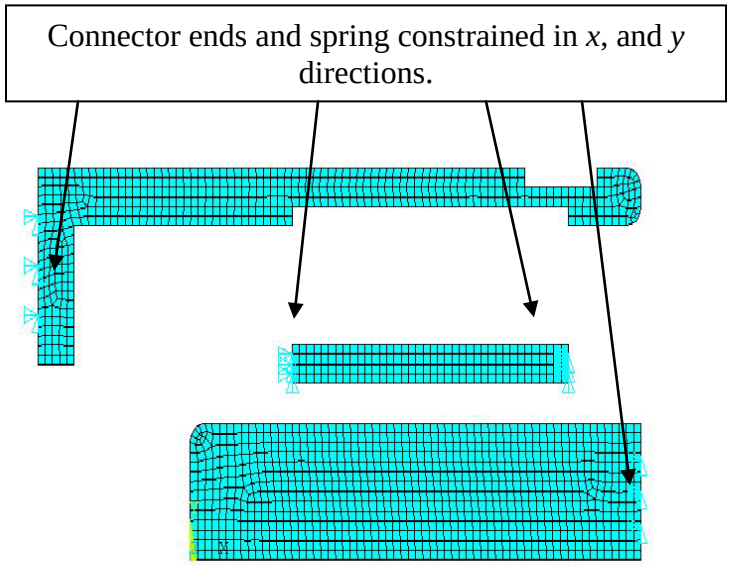

Figure 27 – Structural Boundary Conditions for 2-D Multi-physics FEA.

The leftmost line of the female connector and the rightmost line of the male connector are constrained in the *x* and *y* directions, as shown in Figure 27, since these ends are connected to cables which are held in position by clamps. The spring is constrained in the *x* and *y* directions at both ends. This is done to place the boundary condition on the spring that it cannot move outside of the inside groove on the female end of the connector.

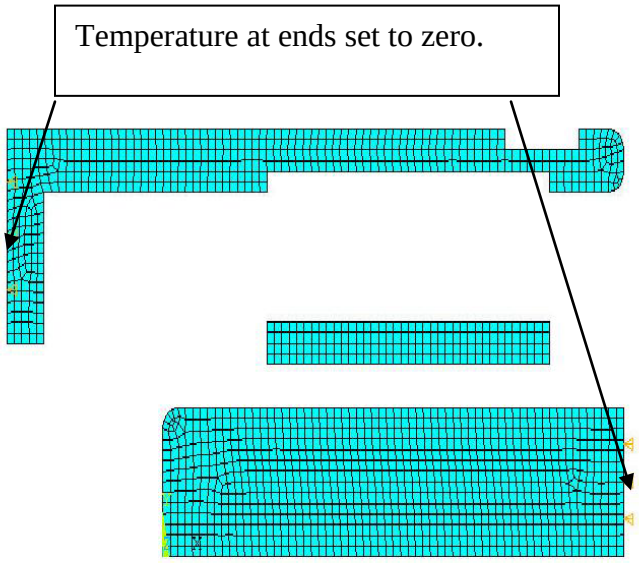

Figure 28 – Thermal Boundary Condition for 2-D Multi-physics FEA.

The temperature at the ends of the female and male ends of the connector are set to zero, as shown in Figure 28. This is done because it is assumed that the temperature in the cable on both sides of the connector will be very close in value. Therefore, the temperature profile across the connector will be a temperature difference relative to the temperature of the connector interface at the cables.

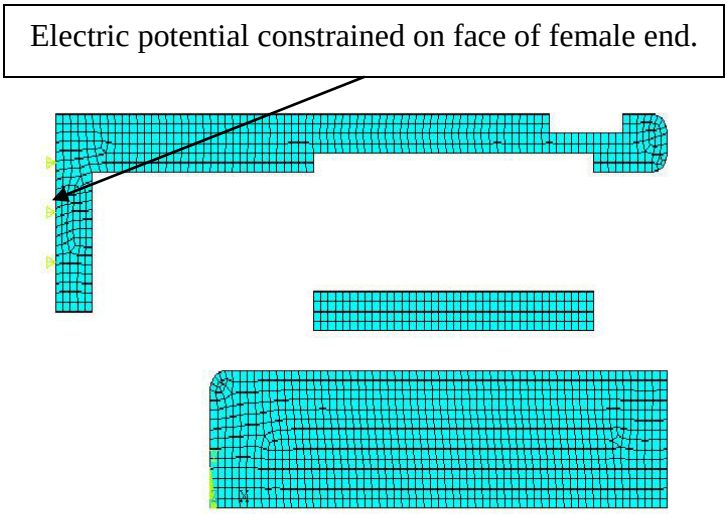

Figure 29 – Electric Potential Boundary Condition for 2-D Multi-physics FEA.

Voltage is held at zero at the leftmost female end of the connector, chosen arbitrarily as the rightmost end of the male connector could be set to zero, to determine the potential distribution across the connector, as shown in Figure 29.

5.5 Methodology of 2-D Multi-physics FEA

The analysis runs in the following order.

1) Set up the geometry of the connector.
2) Set up the material properties for the copper and the composite mass.
3) Set the element type and mesh the geometry with the element types.
4) Apply all structural, electrical, and thermal boundary conditions.
5) Solve the coupled, multi-physics equations using algorithms in ANSYS™.

When setting up the contact using the Link68 elements, adjacent nodes, material properties and cross sectional areas must be provided. The adjacent nodes are found by computing the shortest distance between the node on the composite mass and the node on either the male or female end of the connector. The cross sectional area dictates how

much heat and current can pass through the element. Before the connector is powered, a force balance for the connector system is performed. Using the contact forces, the author determined the contact pressure acting at the interfaces and interpolated, if necessary, the values of ECR and TCR, as given by the Wilson et al. model [30]. The appropriate values of contact pressure, ECR, and TCR are inputted into the Link68 elements accordingly. Once the finite element analysis has converged, ANSYS™ can return displacement, electric potential, temperature distributions, von Mises stress distributions and current density distributions.

CHAPTER 6

Results of 2-D Multi-physics FEA

On average, the 2-D Multi-physics FEA takes only 2-5 minutes to complete. The 2-D Multi-physics FEA can return displacement vector distributions, electrical potential distributions, and temperature distributions. It also has the capacity to return von Mises stress distributions and current density distributions, even though these outputs are not shown in this work.

6.1 General Results

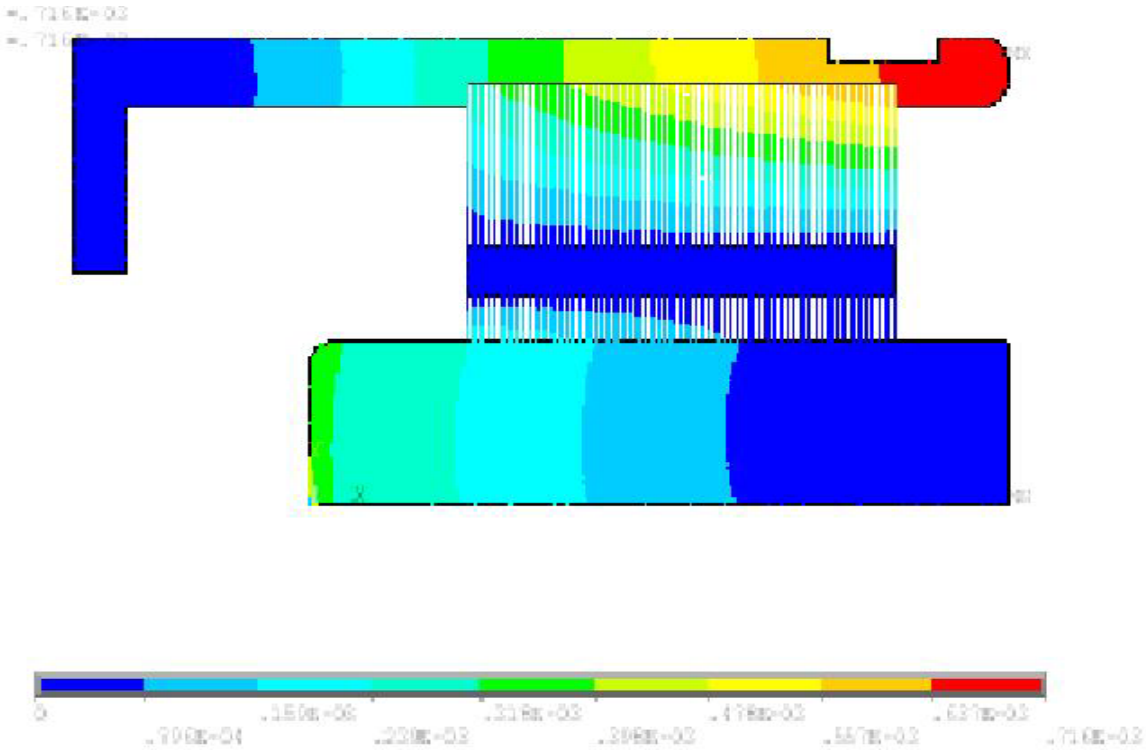

Figure 30 – Displacement Vector Distribution (mm) for Connector at 300A.

Figure 30 shows the displacement vector for the connector when powered at 300A. The scale at the bottom of the picture shows displacements going from

0.8×10^{-4} mm to 0.71×10^{-3} mm. All of the displacements in the connector will be a result primarily of the Joule heating and subsequent rise in temperature. With the current structural boundary conditions, this leads to the ends of the male and female connector parts extending the farthest. When the connector is powered, the spring will also undergo some thermal expansion, but due to the structural constraints to keep the spring in the groove on the inside of the female connector, the spring doesn't deform in same way in the 2-D Multi-physics FEA. Essentially the spring is overconstrained.

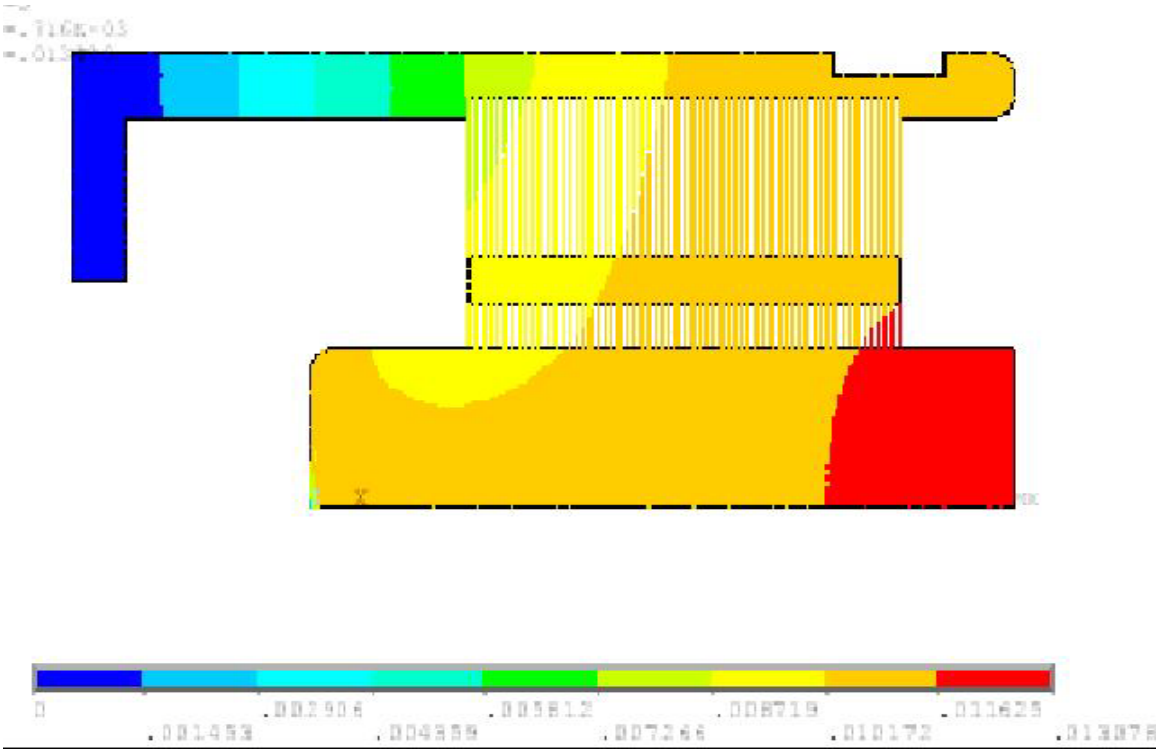

Figure 31 – Electrical Potential Distribution (V) across Connector for 300A.

Figure 31 shows the electrical potential distribution across the connector for 300A. The scale at the bottom of the picture shows potential going from 0.001453 V to 0.01308 V. This distribution for the above mentioned amperage yields an electrical

contact resistance that is within an order of magnitude of agreeing with the experimental results shown later in this work.

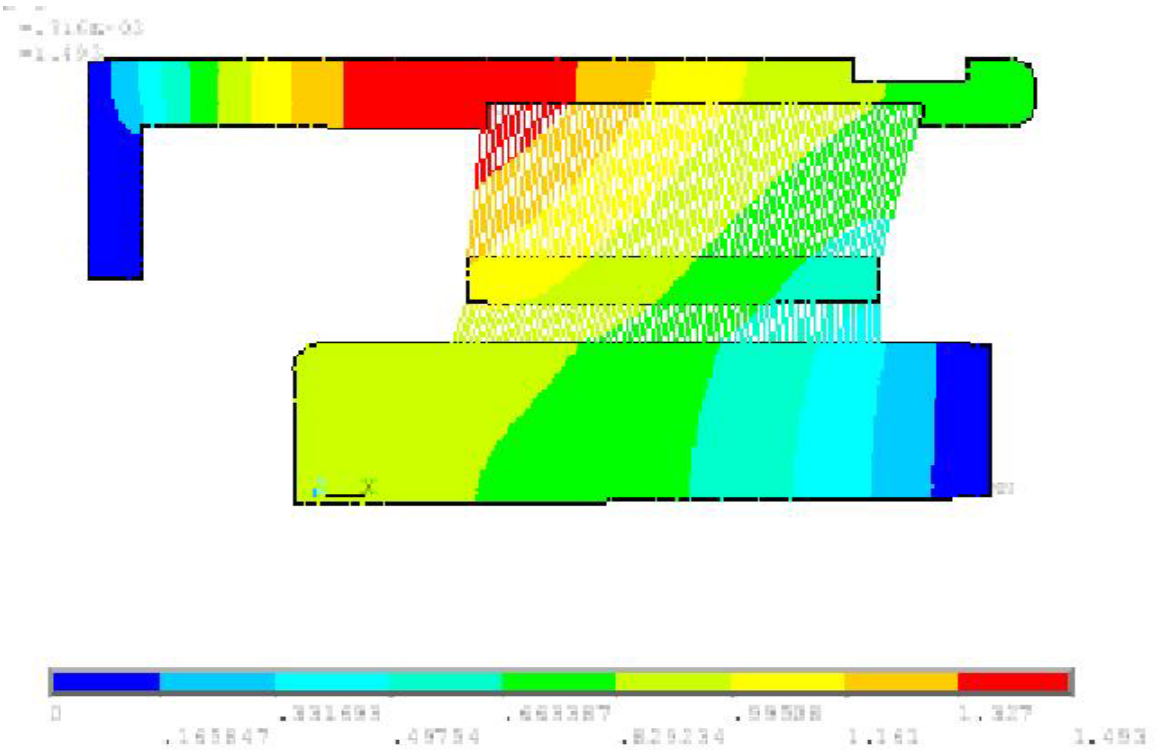

Figure 32 – Temperature Distribution (°C) across Connector for 300A.

Figure 32 shows the temperature distribution across the connector for 300A. The scale at the bottom of the picture shows the temperature going from 0.1658°C to 1.493°C. The temperature distribution shows a localized maximum on the female end of the connector. This localized maximum temperature is within an order of magnitude of agreeing with the experimental results.

6.2 Shortcomings of 2-D Multi-physics FEA

Ultimately, the 2-D Multi-Physics FEA was replaced by the 3-D Multi-Physics FEA because it didn't accurately portray the observed phenomena of electrical contact resistance and temperature distribution in the lab.

While the electrical contact resistance is in agreement by an order of magnitude, the electric potential distribution doesn't agree with the electric potential distribution found in the literature. The current can be thought to travel through several resistors in series: the bulk resistance of the female end of the connector, the electrical contact resistance of the interface between the female end of the connector and the spring, the bulk resistance of the spring, the electrical contact resistance of the interface between the spring and the male end of the connector, and the bulk resistance of the male end of the connector, as shown respectively in Figure 33 and in Figure 34.

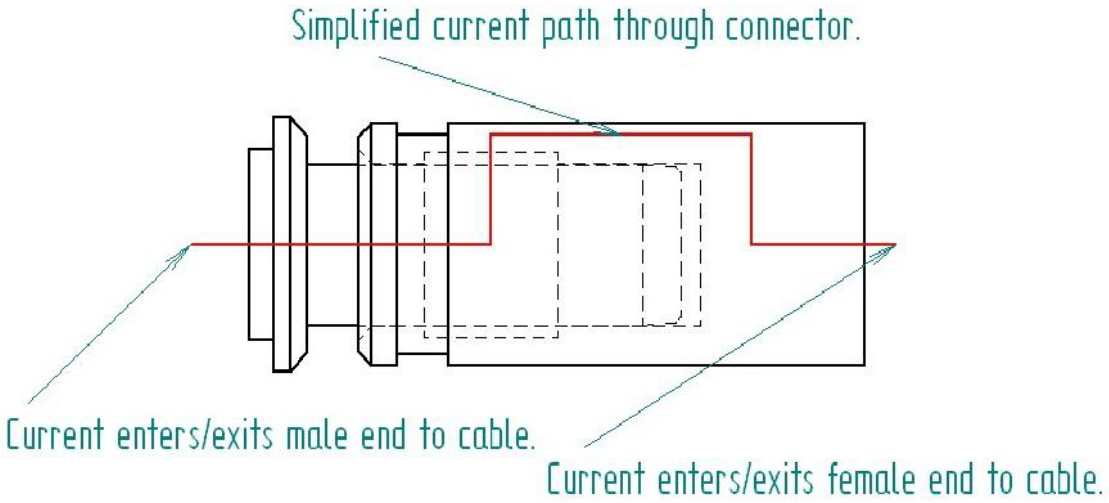

Figure 33 – Path of Current through Round Pin, High Power Connector.

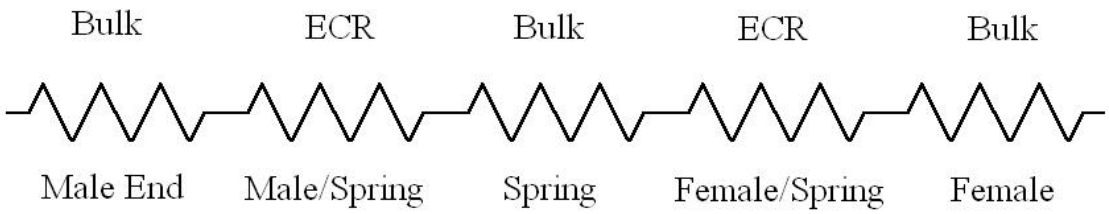

Figure 34 – Series Resistor Network Representation of Round Pin, High Power Connector.

When performing any experiments where electrical contact resistance is measured, the measurements include the above mentioned bulk resistances because it is practically impossible to completely isolate the electrical contact resistance from the bulk resistance of the connector. So examining any voltage drop across the connector will include some bulk resistance. However, constriction resistance and film resistance make up electrical contact resistance, and since the surfaces are considered relatively free of contaminants, electrical contact resistance has to occur because the current must pass through a smaller area. Increasing the current should increase the voltage drop. For the results to be qualitatively correct, the plot of electric potential for the connector should have larger drops near the points of contact. Figure 31, which shows the electrical potential distribution, does not exhibit this behavior. Instead, electrical potential changes regularly across the entire connector with no steep gradients near the points of contact.

This occurs because of the initial assumptions in modeling the contact with the composite mass. Modeling the spring as a composite mass oversimplifies the axi-symmetric, but periodic, geometry of the connector. The profile of the spring changes as one rotates about the axis of symmetry. Some 2-D profiles may have the spring in

contact with the female end of the connector while other 2-D profiles may have the spring in contact with the male end of the connector. In reality, there may be some profiles where the spring is not in contact with either surface. Regardless, the spring has three distinct areas where contact occurs. Using the composite mass, both top and bottom surfaces are assumed to be in contact with the male and female ends.

While the temperature distribution is in agreement by order of magnitude, the temperature distribution profile is not in agreement with the experimental results, as shown in Chapter 3, Round Pin, High Power Connector Experiment. The results show a decreasing trend of temperature from male to female connector parts while the 2-D multi-physics FEA shows an increasing trend to a local maximum near from the edge of the male connector to the spring and male connector end contact and a decreasing trend from the local maximum from the spring and female connector end to the female connector endpoints. This contact pressure, and thus ECR, cannot be modeled accurately using a composite mass.

CHAPTER 7

Setup of 3-D Multi-Physics FEA

A 2-D method was tried first, with hopes that the computational efficiency relative to performing a 3-D analysis would outweigh any shortcomings. When the 2-D method was abandoned due to its shortcomings, a 3-D method was put into its place. It follows the same general methodology for simplifying the entire connector as the 2-D method did but results in a 3-D wedge geometry instead of a 2-D axisymmetric profile.

7.1 Simplification from Connector to 3-D FEA Geometry

In an attempt to simplify the model, and the corresponding computational effort, the model exploits the connector's axi-symmetric periodic nature and analyzes only a small portion of the entire connector system (Figure 4). The connector model in the FEA platform is comprised of a wedge from the male end (Figure 5), a wedge from the female end (Figure 6), and one repeatable section of the spring (Figure 7). The spring sits in a groove on the inside of the female end of the connector, as shown in Figure 11.

7.2 Material Properties

The round pin, high power connector is comprised of three separate parts: the male end, the female end, and the connector spring. All three parts are made of the same materials, an annealed copper with a silver plating finish. The material properties for annealed copper are listed in Table 3. The material properties for silver are listed in Table 1.

7.3 Elements in 3-D Multi-physics FEA

There is a coordinate axis at the lower left hand edge of Figure (35 - 40). The *x*-direction follows the axis of symmetry along the model, the *y*-direction follows the

vertical direction up the page, and the *z*-direction is orthogonal via the right hand rule to the *x* and *y* axes. The model is composed of three element types, Solid226, Targe170, and Conta174. Solid226 elements are multi-physics 3-D brick elements with 20 nodes which allow for a coupled structural, thermal, and electrical analysis. Targe170 elements, composed of a 6 node triangles, specify a 3-D surface that is initially, or will be, penetrated by a Conta element. Conta174 elements, composed of 8 node polygons, represent contact between 3-D target surfaces and a deformable surface, specified by this element. It has the capability of 3-D multi-physics analyses. After meshing, the system contains 15,367 Solid226 elements, 383 Targe170 elements, and 30 Conta174 elements.

7.4 Boundary Conditions in 3-D Multi-physics FEA

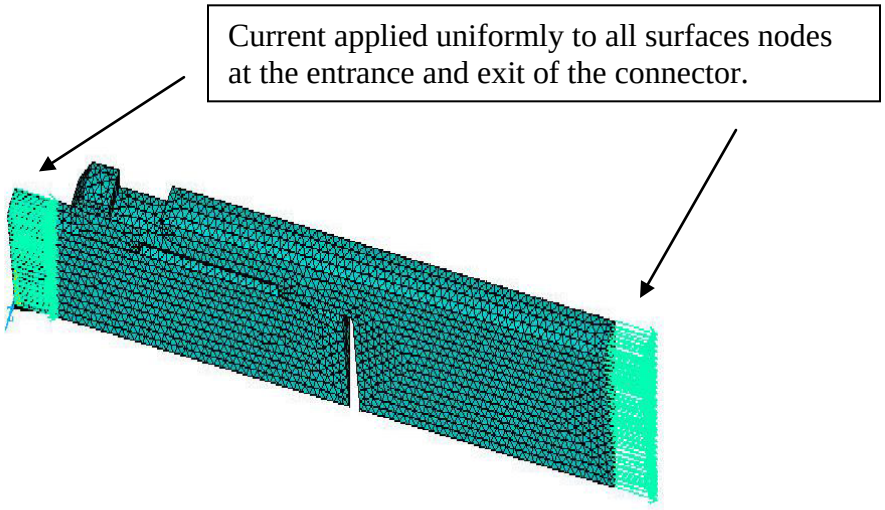

Figure 35 – Current Boundary Conditions for 300A Connector.

The connector is powered with the appropriate amount of uniform current as shown in Figure 35. Current is applied to each node on either end of the male or female connector. In order to determine the current per node, uniform current flux is assumed

for the connector ends. The current then traveling through one period of the connector is the product of the total current flux and the ratio of the cross sectional area of one period to the cross sectional area of the entire end. For either end of the connector, the magnitude of the current traveling through it must be the same although they'll be travelling in the same direction.. The current per node is approximately the ratio of total current passing through the period to the number of nodes on the respective end. Depending on the number of nodes on either face, the current per node may be different.

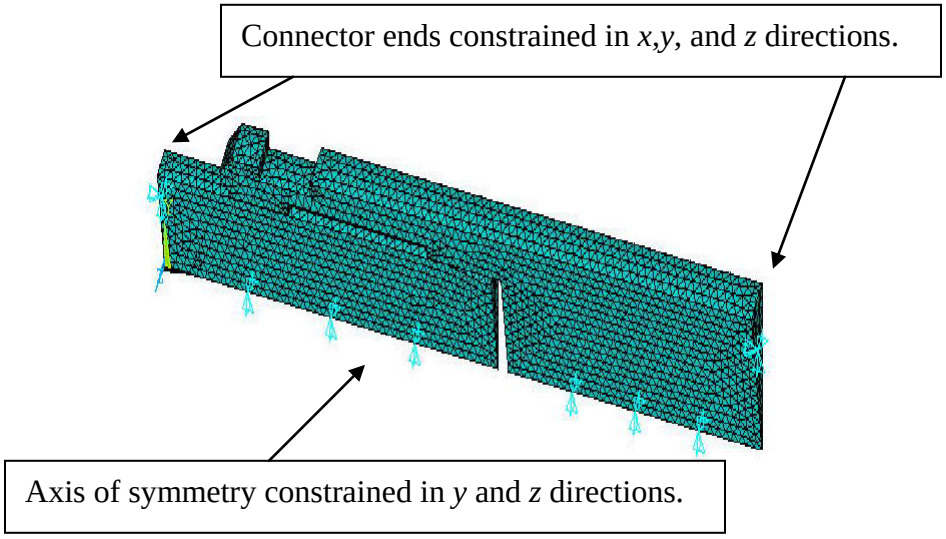

Figure 36 – Structural Boundary Conditions for Connector.

The area of the female connector closest to the cable and the leftmost area of the male connector closest to the cable are constrained in the *x*,*y*, and *z* directions, as shown in Figure 36, since these ends are connected to cables which are held in position by clamps. Also, the axis of symmetry is allowed to move in the *x* direction, as shown in Figure 36, but not in any of the other two orthogonal directions.

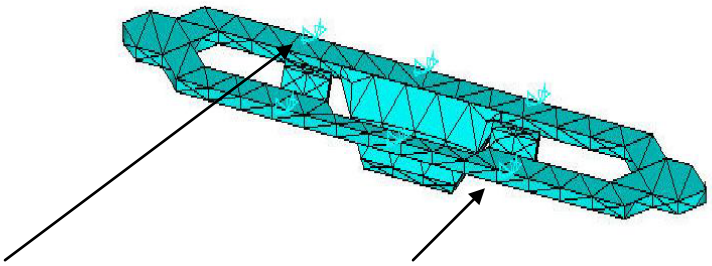

Figure 37 – Structural Boundary Conditions for Spring.

The spring, as shown in Figure 37, may translate vertically in the *y* direction, but the edges are constrained in the *x* and *z* directions. This boundary condition physically keeps the spring in between the male and female ends of the connector. The boundary condition is placed on the two lines making up the edges of the spring, thus allowing the spring to flex while in contact with the male and female ends of the connector. Symmetric boundary conditions are applied in Figure 37 as a way to further model the entire connector system and not just one period.

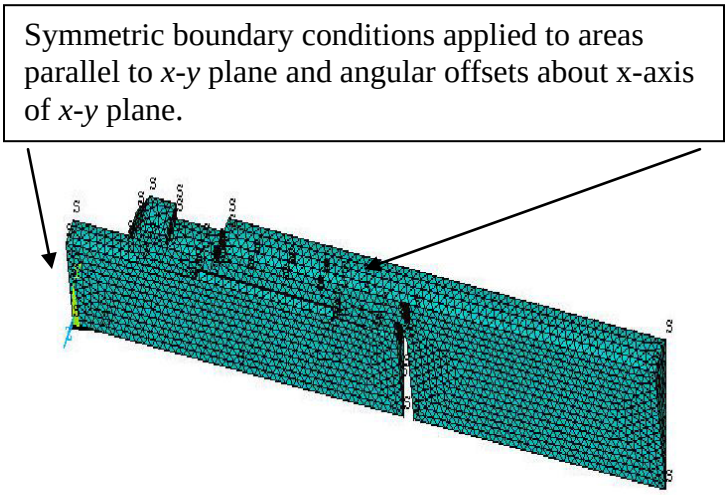

Figure 38 – Symmetric Boundary Conditions on Spring, Male, and Female Ends of the Connector.

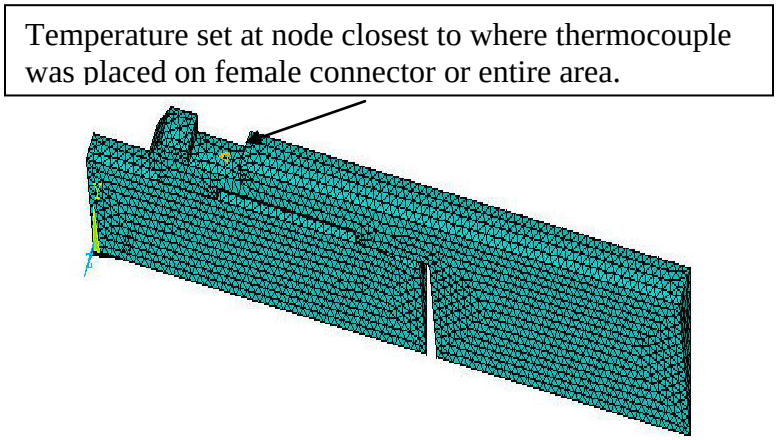

Figure 39 – Thermal Boundary Condition, Determined Experimentally.

The value, position, and type of thermal boundary conditions are set in accordance with experimental results detailed later in this paper. The location of the

thermocouple on the outside groove of the female connector as shown in Figure 39 dictates where the thermal boundary condition is placed. Special care must be taken since thermocouples do not exactly measure the temperature of the object on which they are placed, instead measuring the temperature of the thermocouple. Also, the thermocouple does not measure the temperature at a point but instead of an area on which the thermocouple is attached. Thus, two sets of simulations were run, the first where only the node located closest to the thermocouple was set to the measured temperature of the thermocouple and the second where the area of the groove where the thermocouple was located was set. This is the only thermal boundary condition placed, allowing all other temperature nodes freedom to converge to other values. The simulation does not account for any convective or radiative heat transfer.

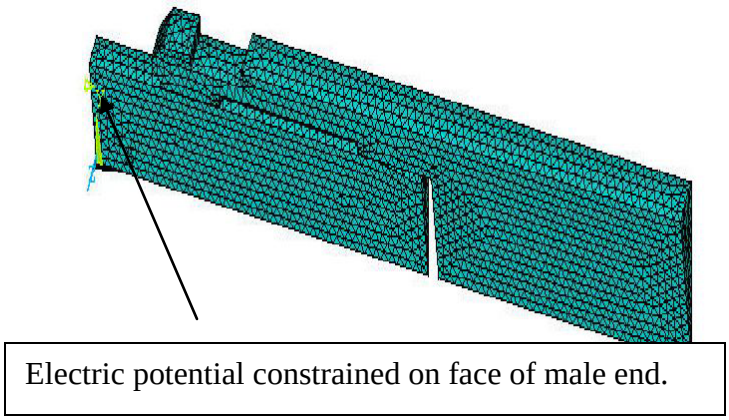

Figure 40 – Electric Potential Boundary Condition on Male End.

Voltage is held at zero at the leftmost male end of the connector, chosen arbitrarily because the opposite end could also be set to zero. In reference to this zero voltage, the potential distribution across the connector, as shown in Figure 40, can be

determined. This will be important when the predicted contact resistance is calculated from the multi-physics FEA results.

7.5 Methodology and Output of the 3-D Multi-Physics Finite Element Analysis

The analysis differs from previous work in that there is no external algorithm determining the convergence of the solution. For instance, in Angadi et al. [40], the contact resistance at each contacting node was determined external to ANSYS™ and updated iteratively. In the current work, the contact resistance is calculated for a variety of pressures using the Wilson et al model [13] before the FEM is started. Once calculated, pressure versus electrical and thermal contact resistance is inserted into ANSYS™ as a table. Thus, all multi-physics coupled field equations are solved internally using ANSYS™. This should lead to faster convergence times in solving the multi-physics finite element analysis as ANSYS™ no longer needs to interface with an outside application like MatLab™.

The steps for performing the 3-D Multi-physics FEA of the round pin connector.

1) Set up the geometry of the connector.
2) Import and place the geometry of the spring.
3) Set up the material properties for copper and silver.
4) Set the element type and mesh the geometry with the element types.
5) Apply all structural, electrical, and thermal boundary conditions.
6) Set up target and contact elements between spring and male connector end using multiscale properties for thermal contact conductance and electrical contact conductance.
7) Set up target and contact elements between spring and female connector end using multiscale properties for thermal contact conductance and electrical contact conductance.
8) Solve using algorithms in ANSYS™.

Once the finite element analysis has converged, ANSYS™ can return displacement, stress, current density, electric potential, and temperature distributions.

CHAPTER 8

Results of 3-D Multi-Physics FEA

On average, the 3-D Multi-Physics FEA 60-90 minutes to complete, which is an order of magnitude in time longer than the 2-D Multi-Physics FEA. The simulations can return displacement, temperature, and electric potential distributions across the entire connector. These predictions are analyzed in the following sections for a variety of input parameters. The parts have been moved after solving the FEA so that there is a line of sight to the spring.

8.1 General Results from 3-D Multi-physics FEA

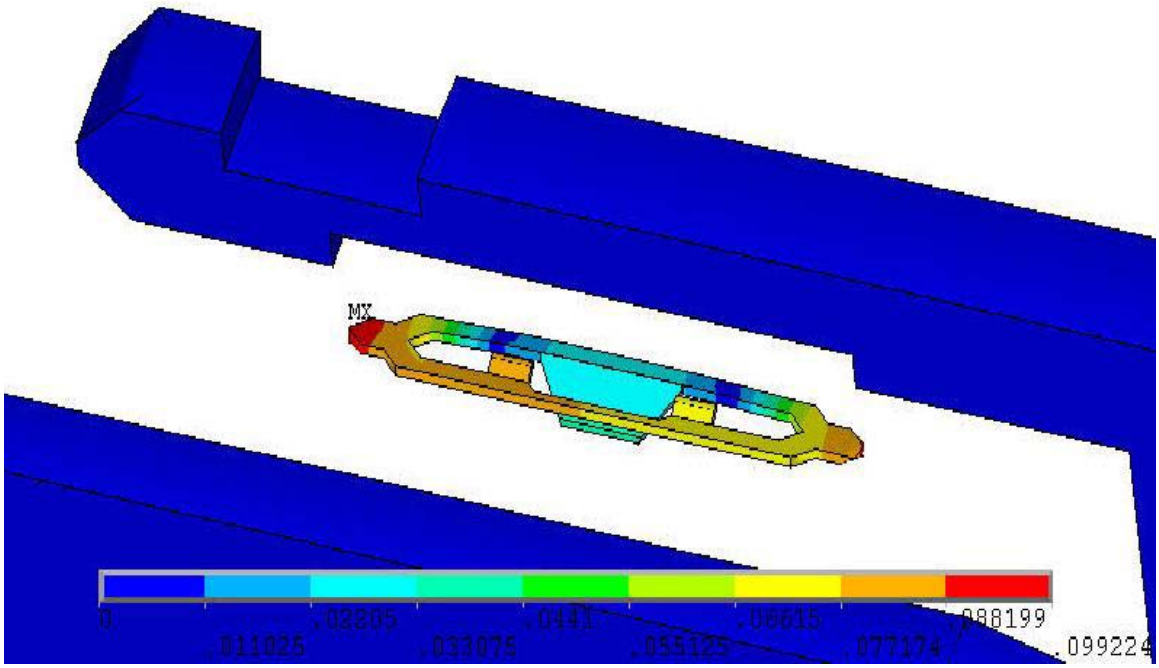

Figure 41 – Displacement Vector Sum (mm) Distribution for Connector with 25 A.

The largest deformations and strains tend to occur in the spring as shown in Figure 42. The analysis begins with the spring being positioned close to its equilibrium location, however, the tabs on the top and bottom of the spring that come into contact with the male and female ends of the connector initially penetrate the surfaces of the male and female ends. The internal ANSYS™ algorithm removes the initial penetration by applying a contact pressure on the tabs via the contact elements, deforming the spring in the multi-physics FEA as it would in reality, and solves the multi-physics coupled field equations. Because of the multi-physics nature of the connector, the displacement vector will depend on the contact forces that act on the spring and from the thermally induced strain due to the temperature rise from Joule heating.

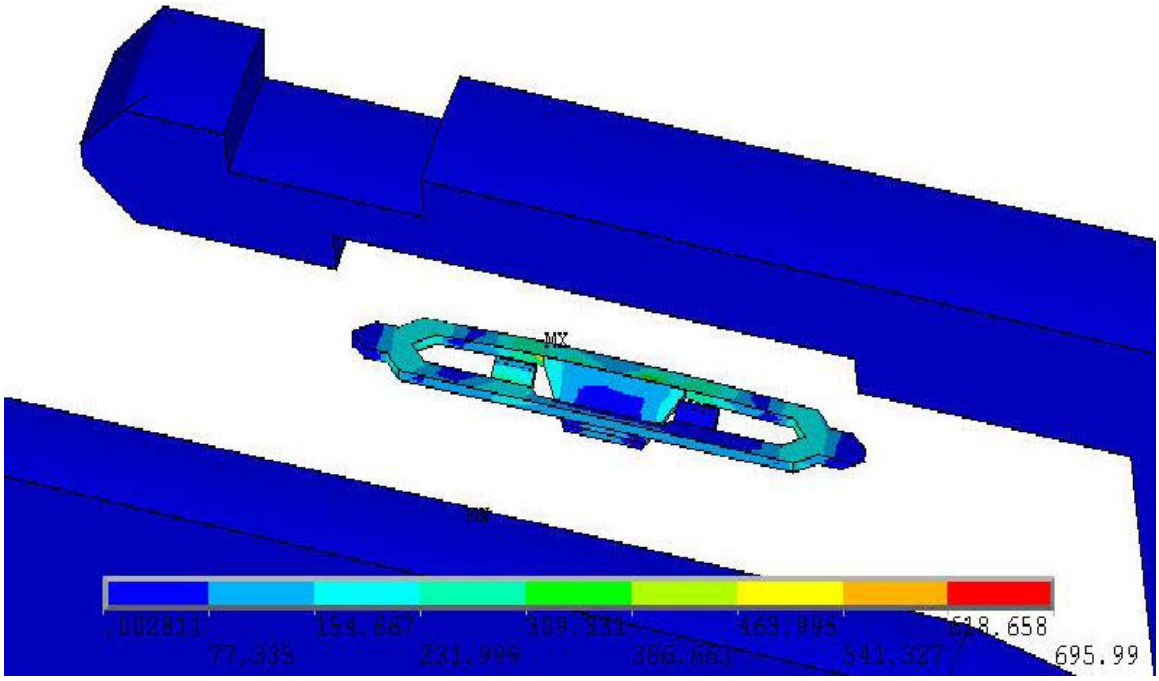

Figure 42 – von Mises Stress (MPa) Distribution in Connector with 25 A.

For a certain current load range, the points of highest stress in the connector system are also localized on the spring, as shown in Figure 42. These points occur at the junctions between the tabs and the rest of the spring. This behavior holds until some amperage between 75-100A when the location changes to the female end of the connector. The stresses in the spring are at least a factor of 10 more than the yield strength of annealed copper. This will be discussed in more detail later.

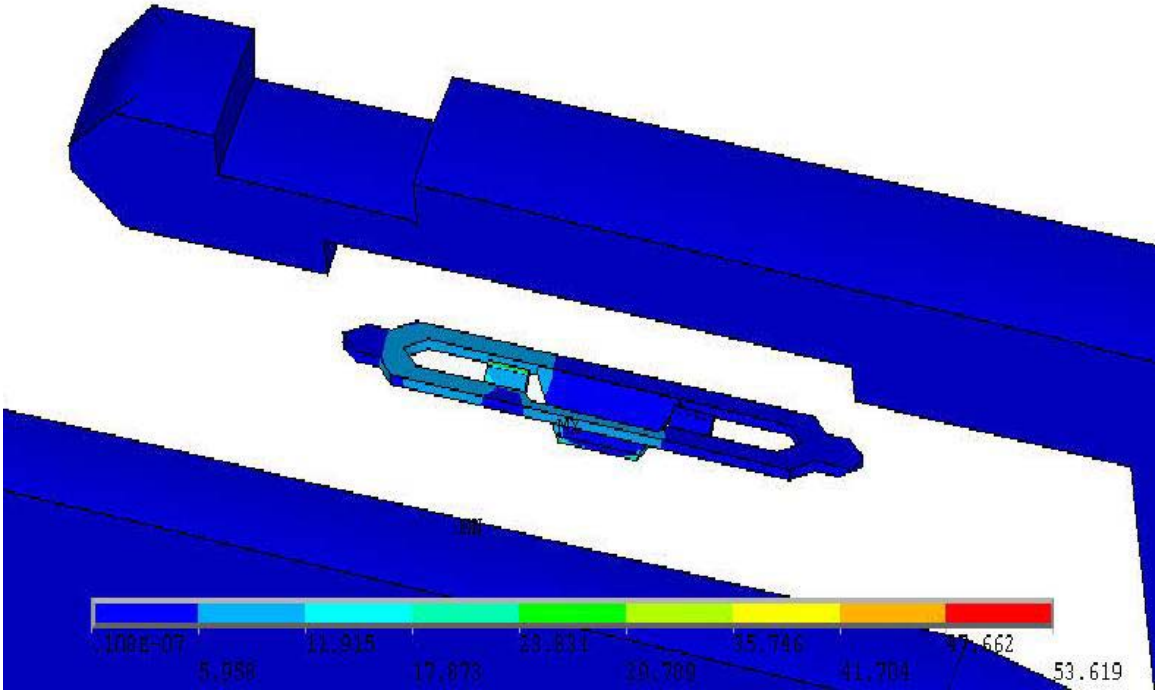

Figure 43 – Current Density, in A/mm², Distribution in Connector with 25 A.

Figure 43 shows current density at its highest concentrations around the areas of contact between the spring and male end of the connector and the spring and female end of the connector. Corresponding to these high current densities, there should be, on a macroscopic scale, a large drop in voltage relative to the surrounding areas due to

constriction resistance. These high current densities could also cause micro or nano-scale localized hot spots on the rough surface of the connector not considered explicitly in the current multi-physics FEA model.

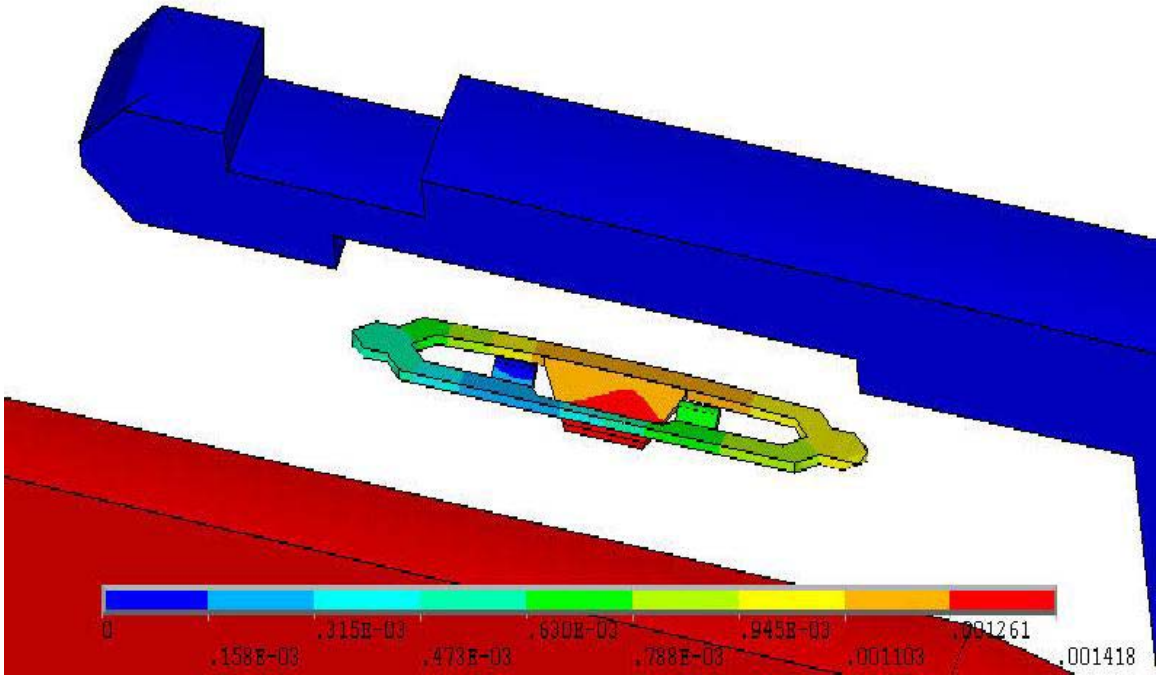

Figure 44 – Electric Potential Distribution (V) across Connector for 25 A.

Figure 44 shows the difference in electric potential that occurs across the spring. This occurs as a result of the increased current density, from Figure 44. Also, both the male end of the connector and the female end of the connector are numerically close to the same electric potential, meaning that bulk resistance in the connector parts can be effectively ignored when measuring the contact resistance of the connector, as most of the resistance occurs across the contacts and the spring.

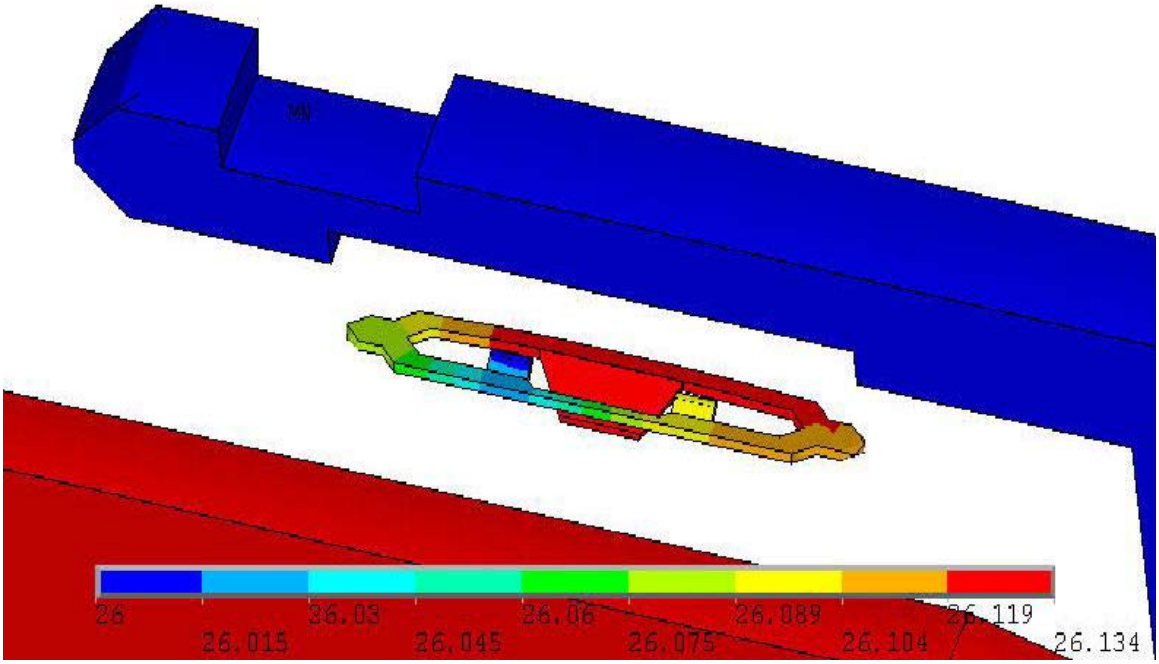

Figure 45 – Temperature Distribution (°C) across Connector for 25 A.

Figure 45 shows the temperature distribution of the connector system. Because of the constraints of the finite element analysis, a node does not exist at the exact point where the thermocouple was placed. Therefore, the temperature at position T2 can be set by setting the temperature of the area of the groove where the thermocouple was placed or by setting the temperature of the node closest to where the thermocouple was placed.

8.2 Correlation between Experimental and Multi-physics FEA Results

In order to validate the 3-D multi-physics FEA, the results obtained from the experiment, mentioned in Chapter 6, and the results obtained from the 3-D multi-physics FEA were compared. The results can be broken into two sections, results from using the ECR properties from the smooth surface and results from using the ECR properties from the smooth and worn surfaces. From each set of properties, one may correlate

experimental and theoretical output like voltage drop and temperature distribution across the connector. Measurement technology employed in this project yielded connector resistance and temperature. Because of these limitations, the 3-D multi-physics FEA became useful in predicting such results as current density and stress distributions.

8.2.1 Results for Connector Resistance

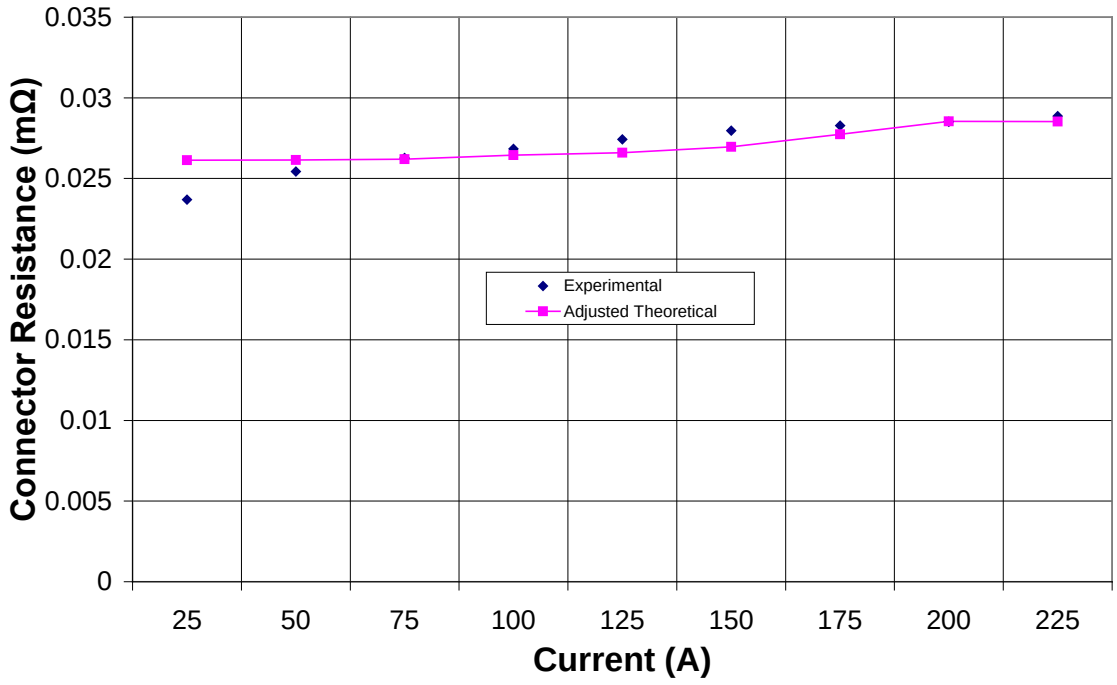

Figure 46 – Connector Resistance for Area Thermal Boundary Condition vs. Current.

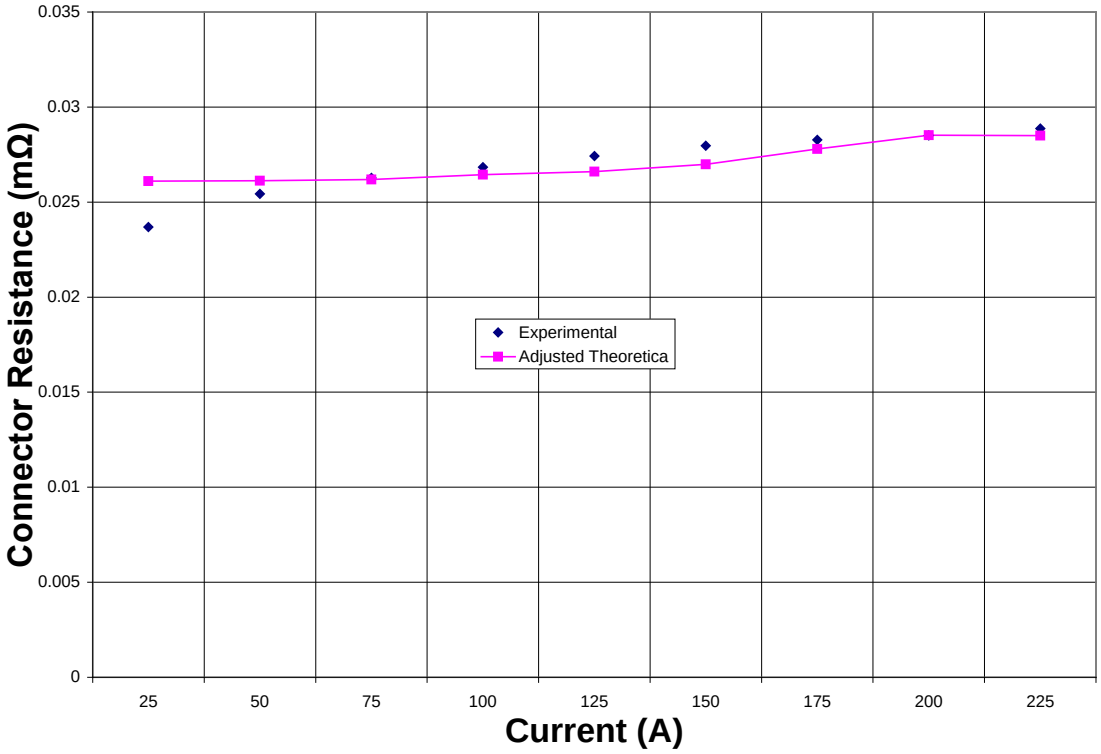

Figure 47 – Connector Resistance for Nodal Thermal Boundary Condition vs. Current.

Total connector resistance values are calculated by dividing the potential difference across the entire connector by the total current that goes through the connector. The connector resistance values for FEA, as shown in Figure 46 and Figure 47, are then adjusted by taking the average of both FEA and experimental data, finding the difference between the averages, and subtracting that difference from the FEA data. The adjustment corresponds to an offset occurring due to the possible difference in the bulk resistance between the model and the experiment. With this adjustment, the FEA data and experimental results agree closely, both in magnitude and a trend towards increasing contact resistance with increasing current. Bulk resistance isn't increasing with temperature because temperature dependent material properties aren't included in the

model. This overall increase in connector resistance must be coming from the contacts. Thermally induced warping in the spring could be responsible for shrinking the area of contact and thus increasing the electrical contact resistance. Another possibility is the radial expansion of the female end. If the radial displacement of the groove on the inner part of the female end is greater than the radial displacement of the top of the male end, then the connector parts will not be as close together, thus decreasing the contact reaction forces on the spring and thus increasing the electrical contact resistance.

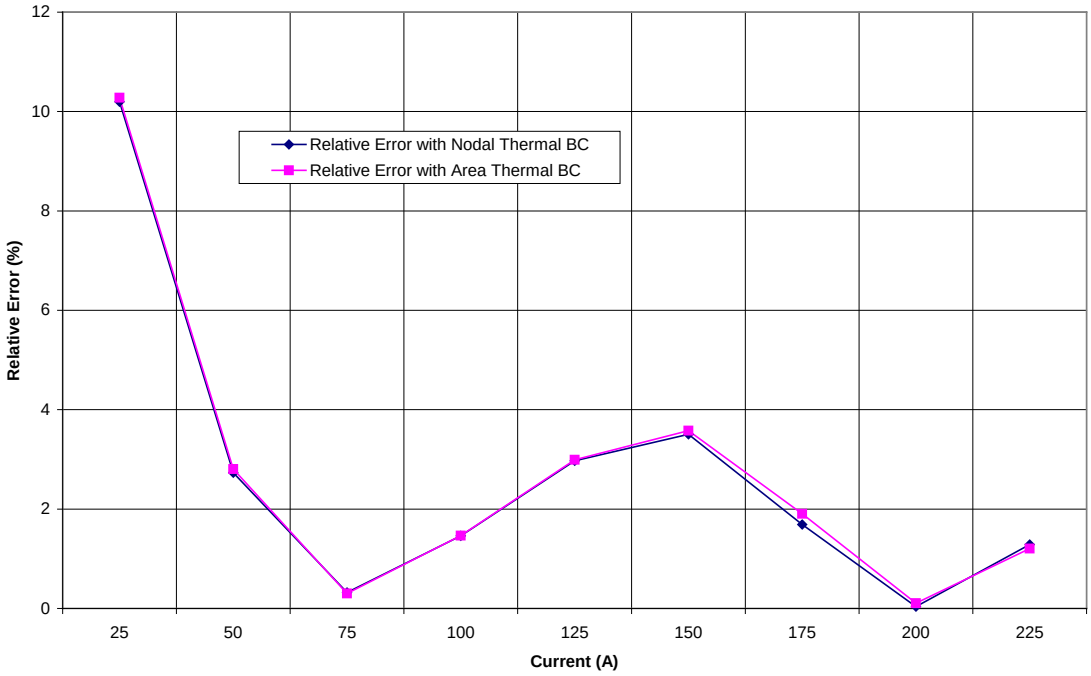

Figure 48 – Relative Error between Experimental and Theoretical ECR for Area and Nodal Thermal Boundary Condition.

Figure 48 shows the relative error between the theoretical contact resistance and the measured contact resistance for both thermal boundary conditions. For the area

thermal boundary condition, the maximum relative error is 10.2789%, and the average error is 2.7372%. For the nodal thermal boundary condition, the maximum relative error is 10.1979%, and the average error is 2.6895%. Since relative errors are sufficiently close, the thermal constraints on the connector system appear to have little influence on the electrical results (contact resistance and current density). Thus, when determining contact resistance or current density, either boundary condition will suffice.

8.2.2 Results for Temperature Distributions

The temperatures of the thermocouples at Position 1 and Position 3 are detailed in Figure 11 and Figure 12. The temperature plots below are the temperature of the node returned from the simulation closest to where the thermocouple would have been placed.

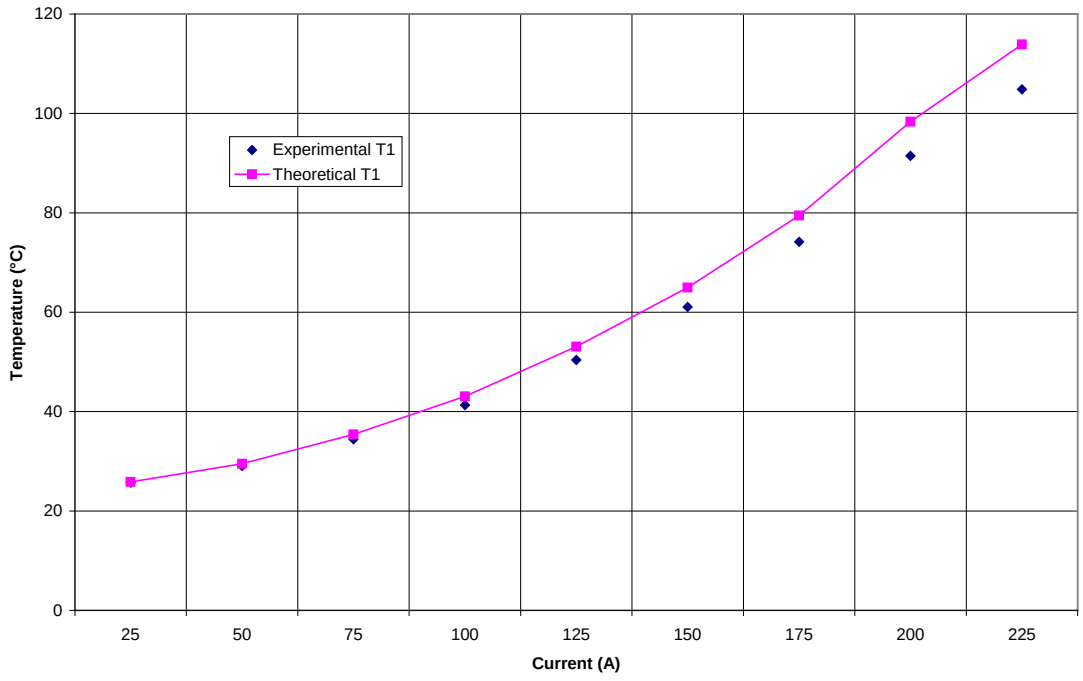

Figure 49 – T1 with Area Thermal Boundary Condition vs. Current.

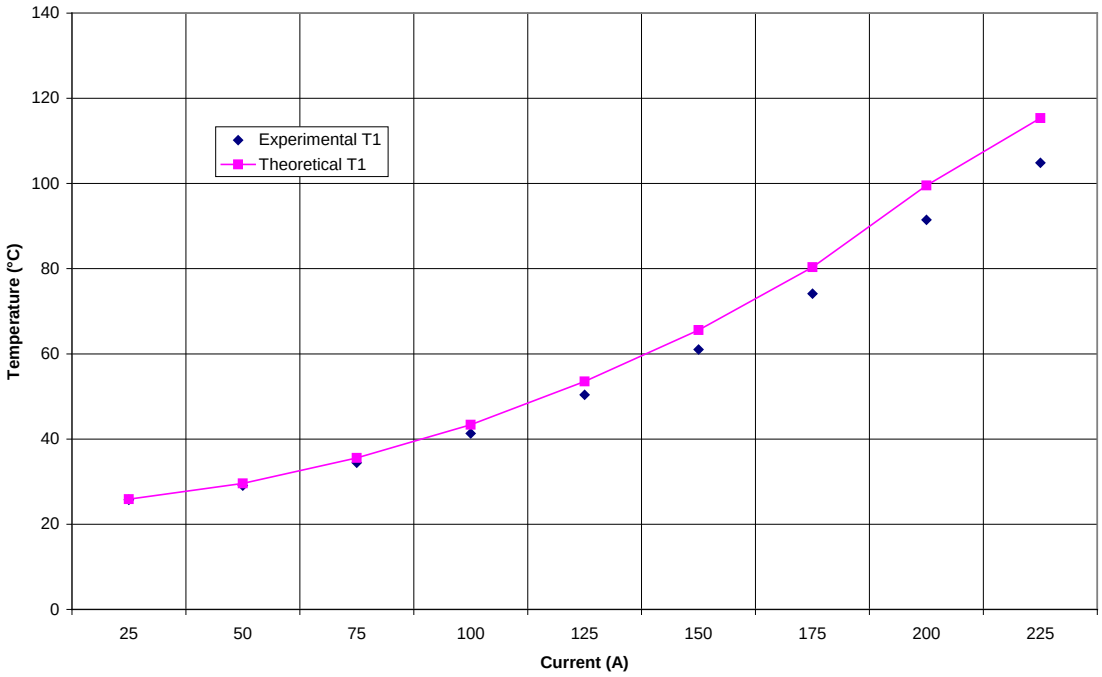

Figure 50 - T1 for Nodal Thermal Boundary Condition vs. Current.

Figure 49 shows the relation between the measured temperatures and the theoretical temperatures at Position 1 for the area thermal boundary condition. Figure 50 shows the relation between the measured temperatures and the theoretical temperatures at Position 1 for the nodal thermal boundary condition. Both sets of theoretical temperatures follow the same increasing trend as the experimental temperatures. This data follows the expected trend for Joule heating of the connector system. As current load is increased, the heat generated is increased non-linearly. Given the absence of convective and radiative heat transfer, increasing current should lead to increasing heat, which leads to increasing temperatures

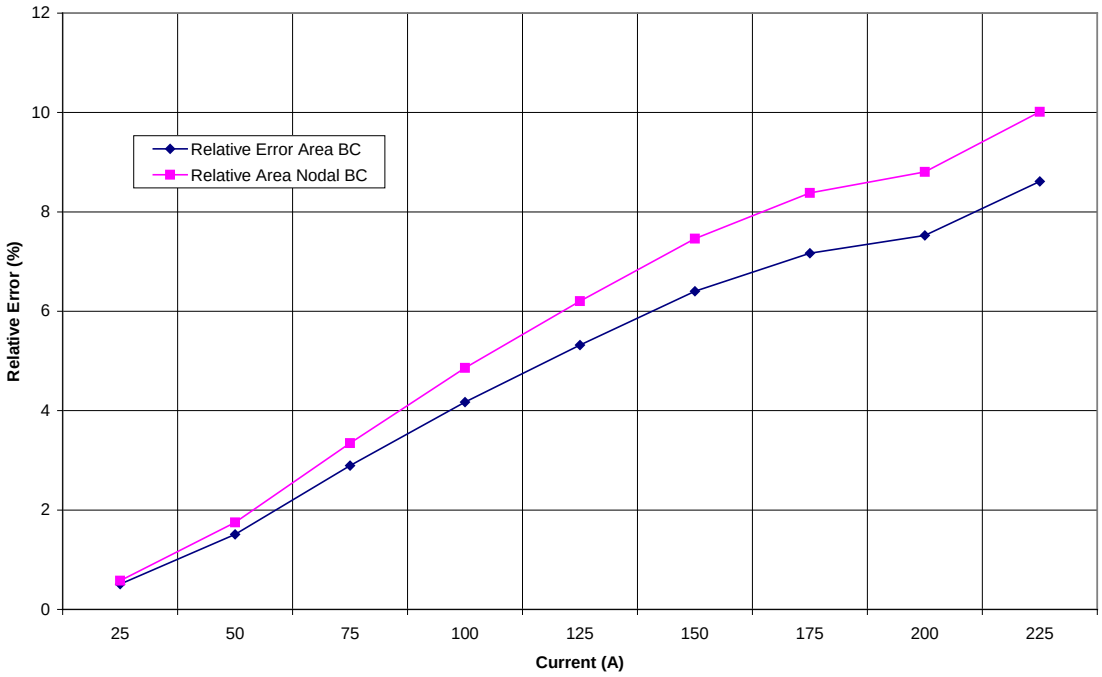

Figure 51 – Relative Error of Temperature at Position 1 for Area and Nodal Boundary Conditions vs. Current.

In Figure 51, both sets of relative errors, for area and nodal thermal boundary conditions, increase with increasing temperature. For the area thermal boundary condition, the maximum relative error is 8.623%, and the average relative error is 4.9019%. For the nodal thermal boundary condition, the maximum relative error is 10.0143%, and the average relative error is 5.7107%. The relative error for the area thermal boundary condition increases at a lower rate than the relative error for the nodal boundary condition. Therefore, the area thermal boundary condition is the better choice for usage in the 3-D multi-physics FEA. This occurs because of the number of nodes set to the experimentally measured value at Position 2. In the nodal thermal boundary case,

only one thermal node is set. However, in the area thermal boundary case, the entire area of the groove where the second thermocouple is placed is set to the same temperature. Because the temperature value of any node depends on the neighboring nodes, the thermal effect of having many nodes set to the experimentally determined value is greater than the thermal effect of having one node set to the experimentally determined value. Also, the connector system in reality is subject to heat transfer via convection and radiation. Since these factors are not included in the analysis, the connector can be seen to be perfectly insulated at its surface; therefore, it should not be surprising that the temperature at the other thermocouple locations is slightly higher than the experimentally determined values.

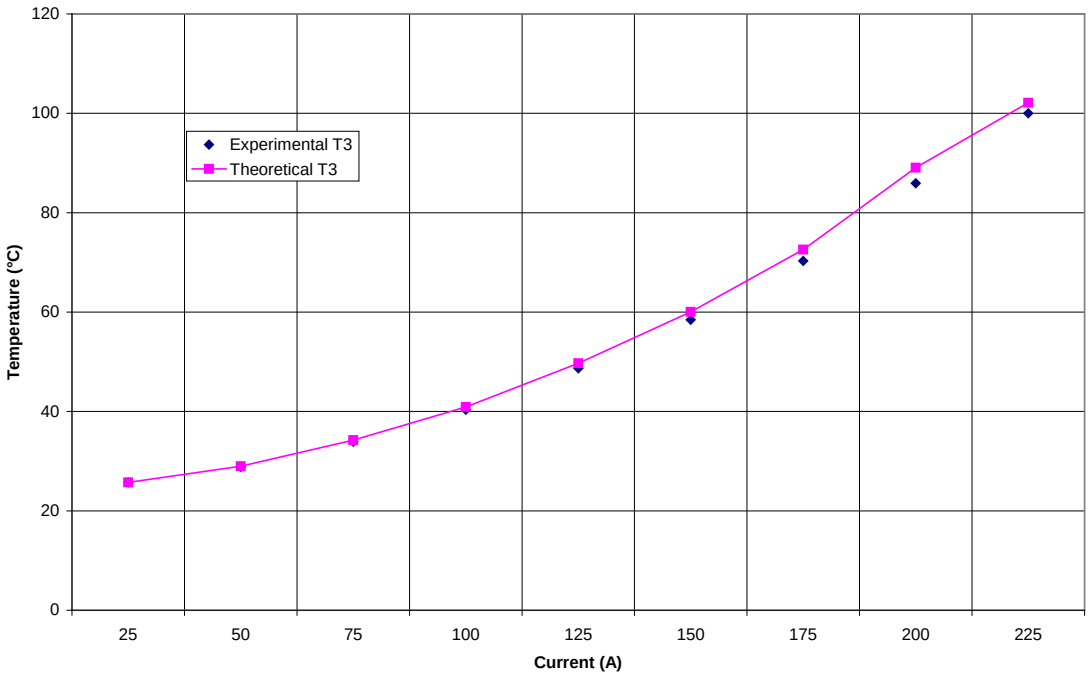

Figure 52 – T3 for Area Thermal Boundary Condition vs. Current.

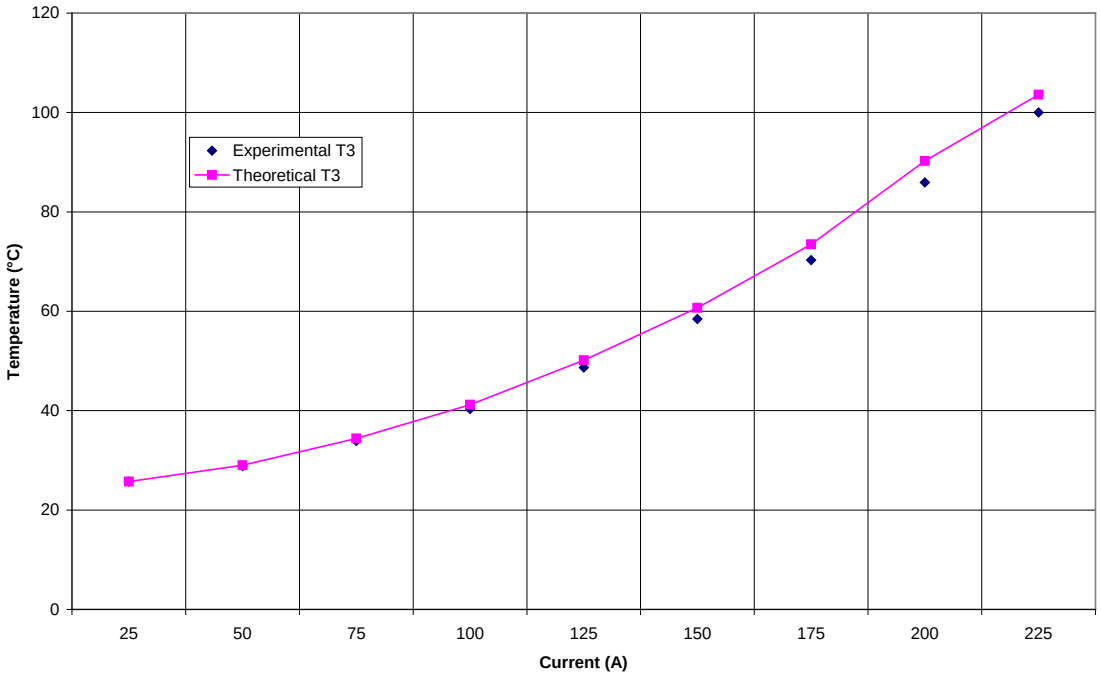

Figure 53 – T3 for Nodal Thermal Boundary Condition vs. Current.

Figure 52 shows the relation between the measured temperatures and the theoretical temperatures at Position 3 for the area thermal boundary condition. Figure 53 shows the relation between the measured temperatures and the theoretical temperatures at Position 3 for the nodal thermal boundary condition. Both sets of theoretical temperatures follow the same increasing trend as the experimental temperatures.

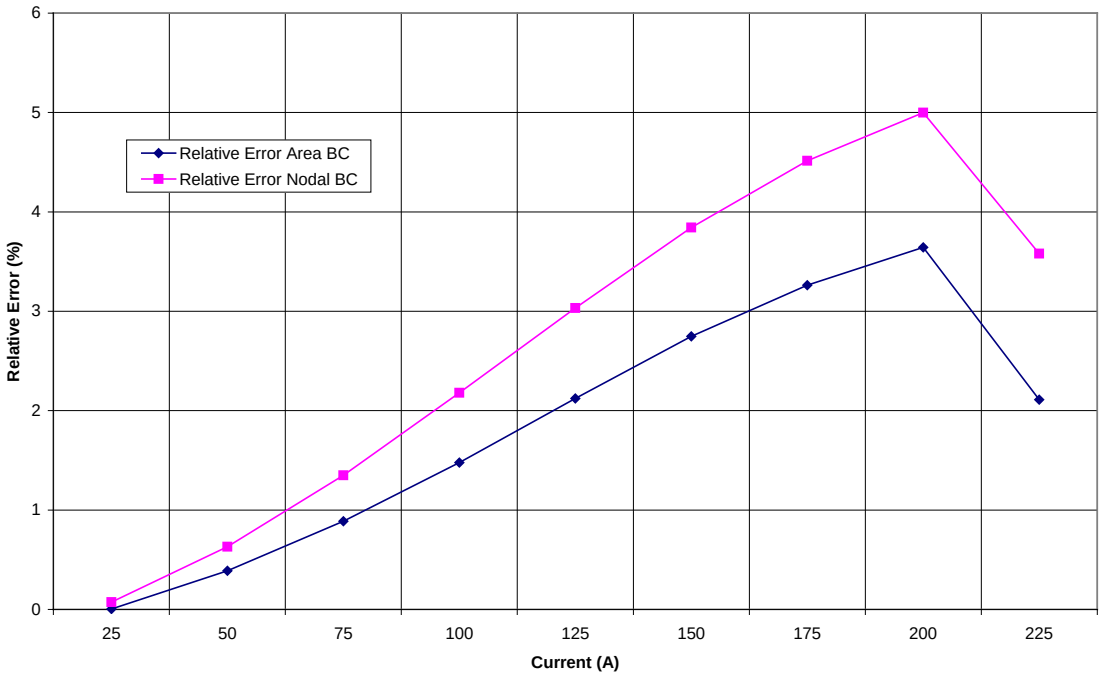

Figure 54 – Relative Error of Temperature at Position 3 for Area and Nodal Thermal Boundary Condition vs. Current.

In Figure 54, both sets of relative errors, for area and nodal thermal boundary conditions, increase with increasing temperature. Like the thermal behavior at position 1, the relative error for the area thermal boundary condition increases at a slightly lower rate than the relative error for the nodal boundary condition. For the area thermal boundary condition, the maximum relative error is 3.6425%, and the average relative error is 1.8494%. For the nodal thermal boundary condition, the maximum relative error is 4.9983%, and the average relative error is 2.6889%. Therefore, the area thermal boundary condition appears to be a better choice for usage in the 3-D multi-physics FEA.

8.2.3 Results for Normalized Current Density

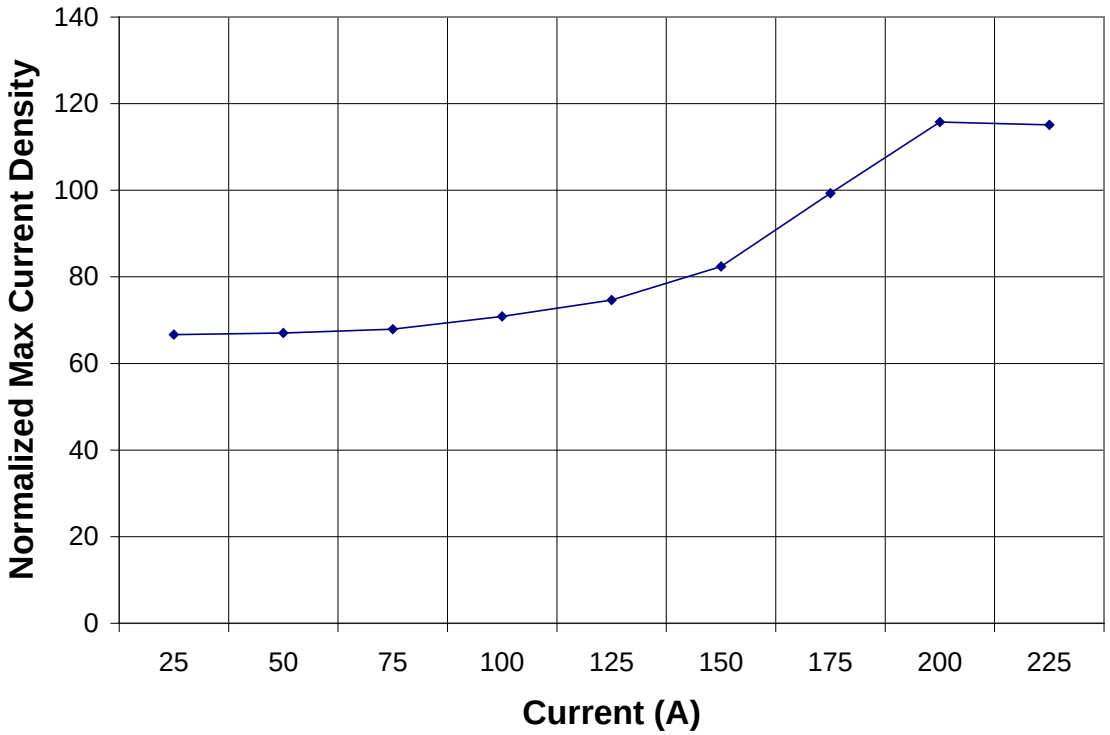

Figure 55 – Normalized Maximum Current Density vs. Current.

Figure 55 is a plot of applied normalized maximum current density vs. current. The maximum current density is found from an output list of current density through each Solid 226 element. The average current density is found by summing the current density at each node and dividing by the number of nodes. The maximum current density is then normalized by the average current density. The above plot shows an increasing trend for normalized maximum current density with increasing current, meaning that the current is not diffusing out into the connector. As shown in Figure 56, these high current densities are occurring at the interface of the spring and the connector. With these high current densities, thermally induced asperity deformation would more readily occur at a location in the connector where wear and deformation are already a problem. Note that these high

current densities might also not be predicted for simplified connector models which assume a uniform current distribution.

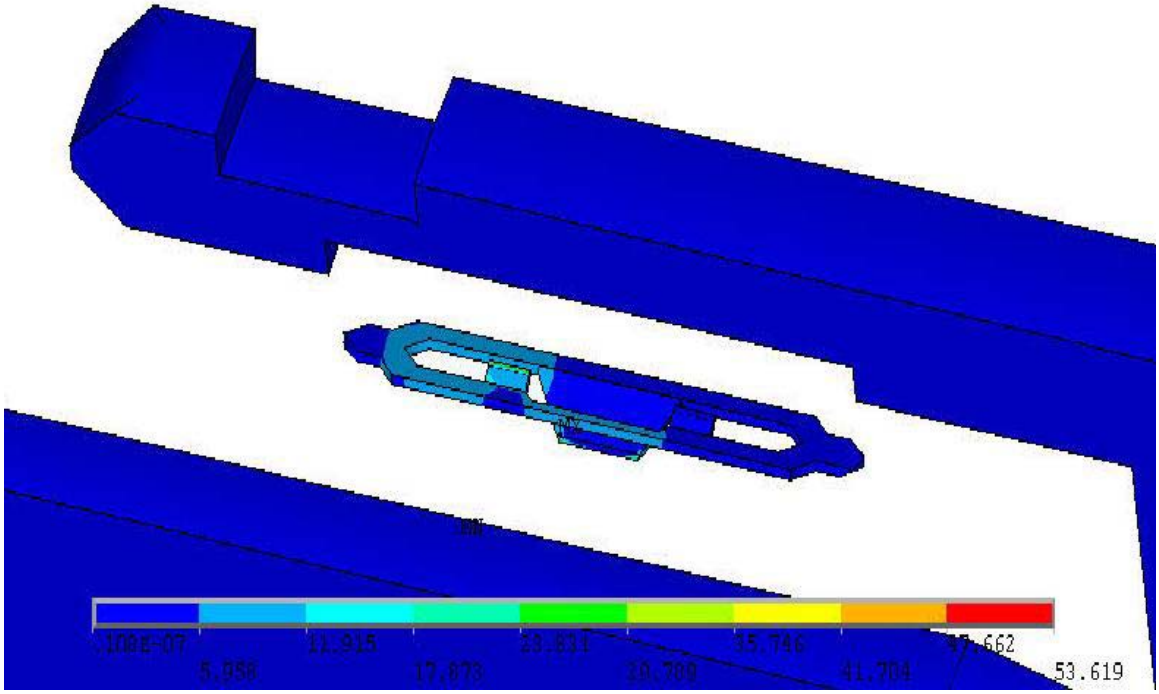

Figure 56 – Current Density Distribution (A/mm²) across Connector for 25 A.

8.2.4 Results for Maximum von Mises Stress

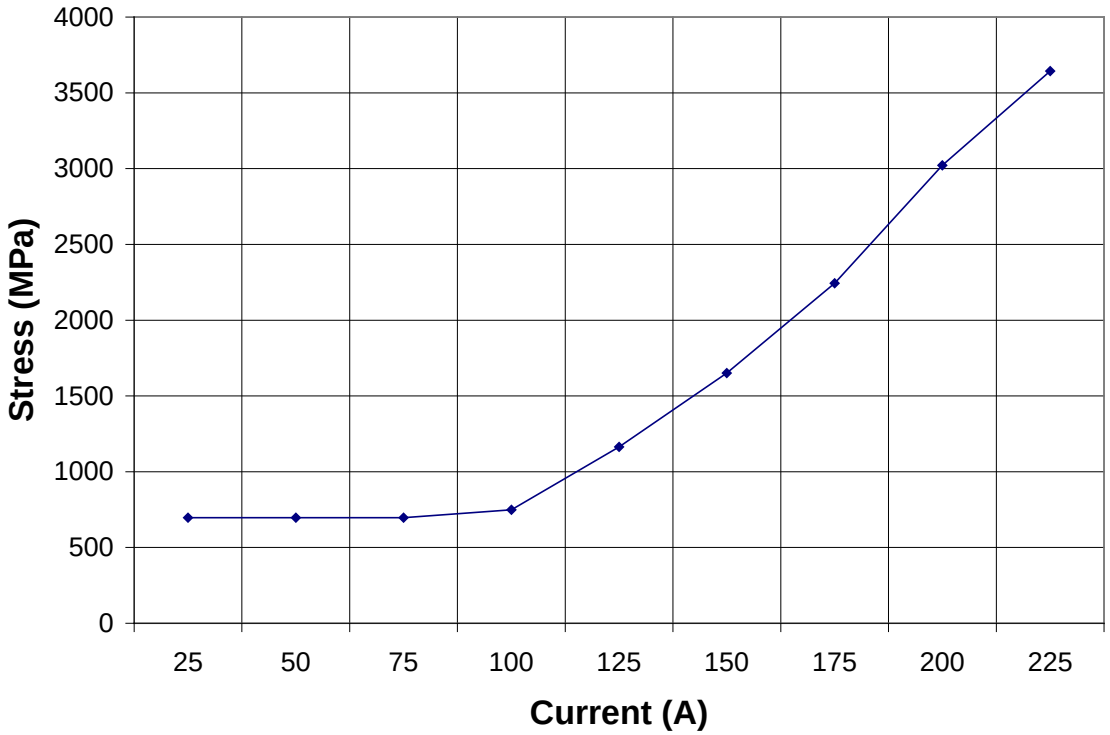

Figure 57 –Maximum von Mises Stress vs. Current.

Figure 57 shows the relationship between current and the maximum value of the von Mises stress in the connector. The maximum value of the von Mises stress holds nearly steady until 100A when it begins to increase with increasing current. For currents between 25A – 75A, the location of the maximum von Mises stress is on the spring, as shown in Figure 58. However, the location of the maximum von Mises stress changes from the spring to the axis of symmetry on the female end of the connector, as shown in Figure 59. This could be due to the structural boundary conditions on the ends of the connector. These stresses are very high and if they do exist in the connector under these operating conditions, they will certainly cause yielding.

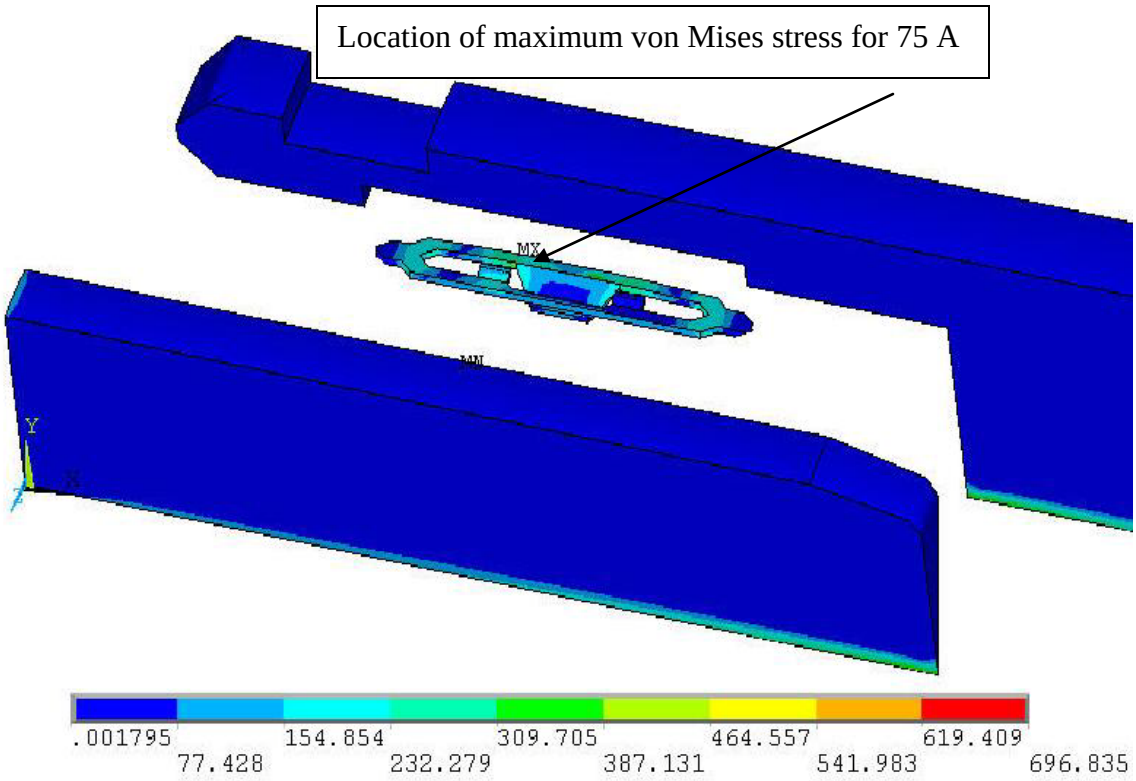

Figure 58 – von Mises Stress Distribution for 75A.

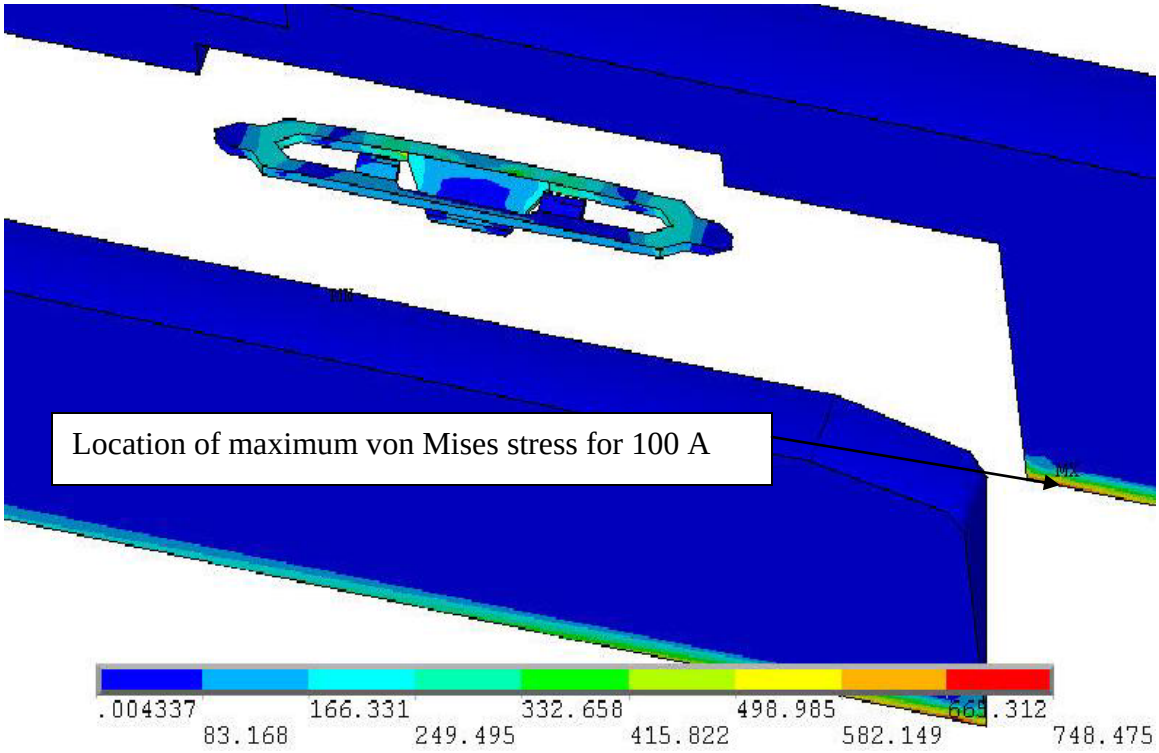

Figure 59 – von Mises Stress Distribution for 100A.

8.3 Prediction of Results when Increasing ECR

The multi-physics FEA results outlined in 8.2 are correlated to the experimental results outlined in Chapter 3. Both results are for a steady-state, static analysis. Since this connector system has applications in automotive vehicles, it will be subjected to vibrations during vehicle operation. These vibrations will cause relative motion between the contact interfaces of the connector system, leading to fretting of the surface and an increase in electrical contact resistance. Doing this dynamically in a FEA would require the finite element software to solve the equations of motion of each part in the connector system, to keep track of the material removed due to wear and update the geometry accordingly, and to solve the coupled thermo-electrical equations. The surface roughness

and change in chemistry at the surface would also have to be predicted, which is not currently and theoretically feasible. Instead of engaging in this computationally expensive process, one could instead quickly examine the connector using artificially increased electrical contact resistance properties.

In this section, current will be held constant at 225A, but ECR and TCR values, as functions of contact pressure, will incrementally increase. Finally, these results will be compared with the predictions from using the multi-scale properties from two worn surfaces from actual used connectors.

8.3.1 Methodology of Increasing ECR

While maintaining a constant current value of 225A, ECR and TCR values, as predicted by the Wilson et al. multiscale method [30], are artificially increased by 10%, 20%, 30%, 40%, 200%, and 300%. This is done to predict the behavior of the maximum temperature of the connector, the electrical contact resistance across the connector, the maximum von Mises stress, and the normalized maximum current density for the connector as if it were failing. All results increase for increasing electrical contact resistance properties.

8.3.2 Results of Increasing ECR

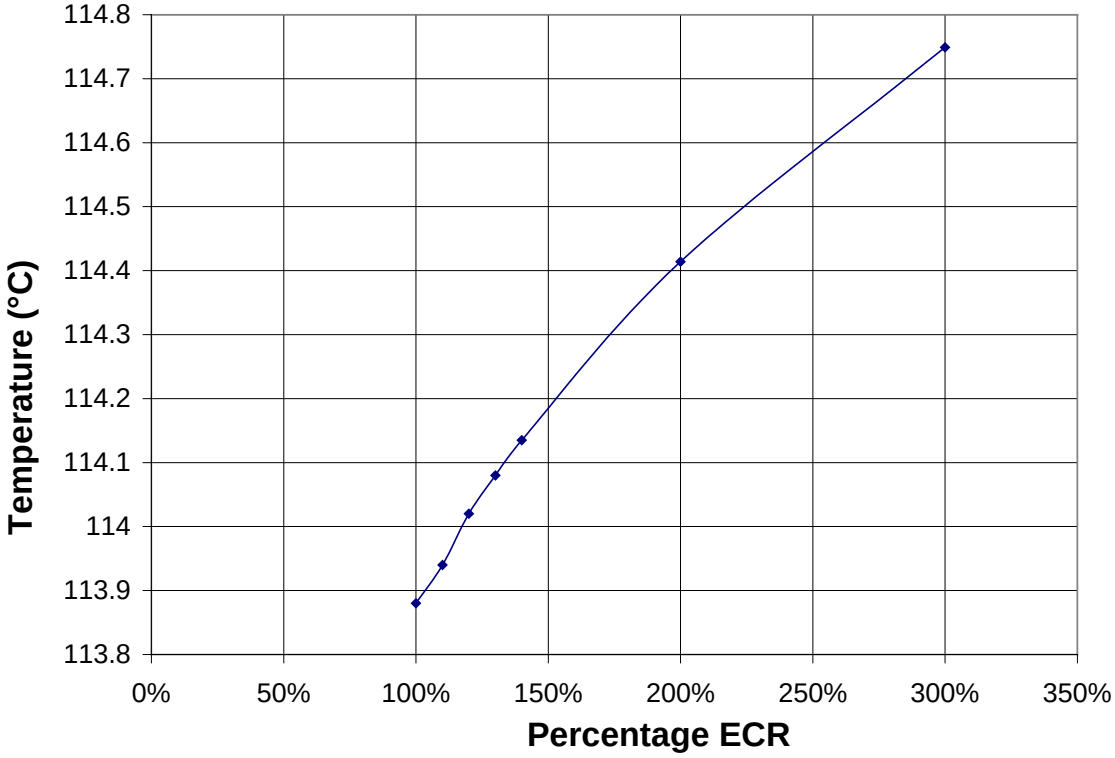

Figure 60 – Maximum Temperature vs. Percentage Increase ECR.

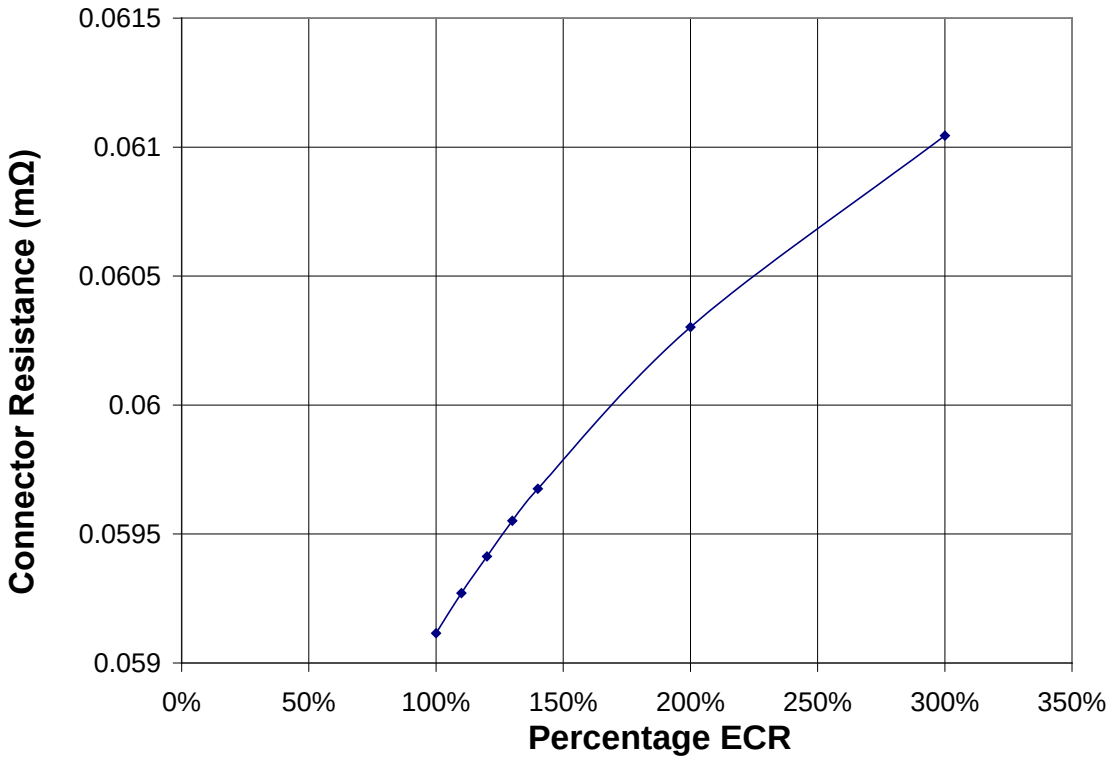

Figure 61 –Connector Resistance vs. Percentage Increase ECR.

As expected, increasing the electrical and thermal contact resistance properties will cause an increase in the maximum temperature of the connector, as shown in Figure 60, and an increase in the electrical contact resistance across the connector system, as shown in Figure 61. As the electrical contact resistance values are increased, the current will have to pass through a larger electrical contact resistance, leading to an increase in connector resistance. As the thermal contact resistance values are increased, and the heat could become trapped, if the thermal contact resistance is higher than the surrounding bulk thermal conductivity. If heat becomes trapped, then higher temperatures should occur. The maximum temperature occurs for each increase in ECR on the spring.

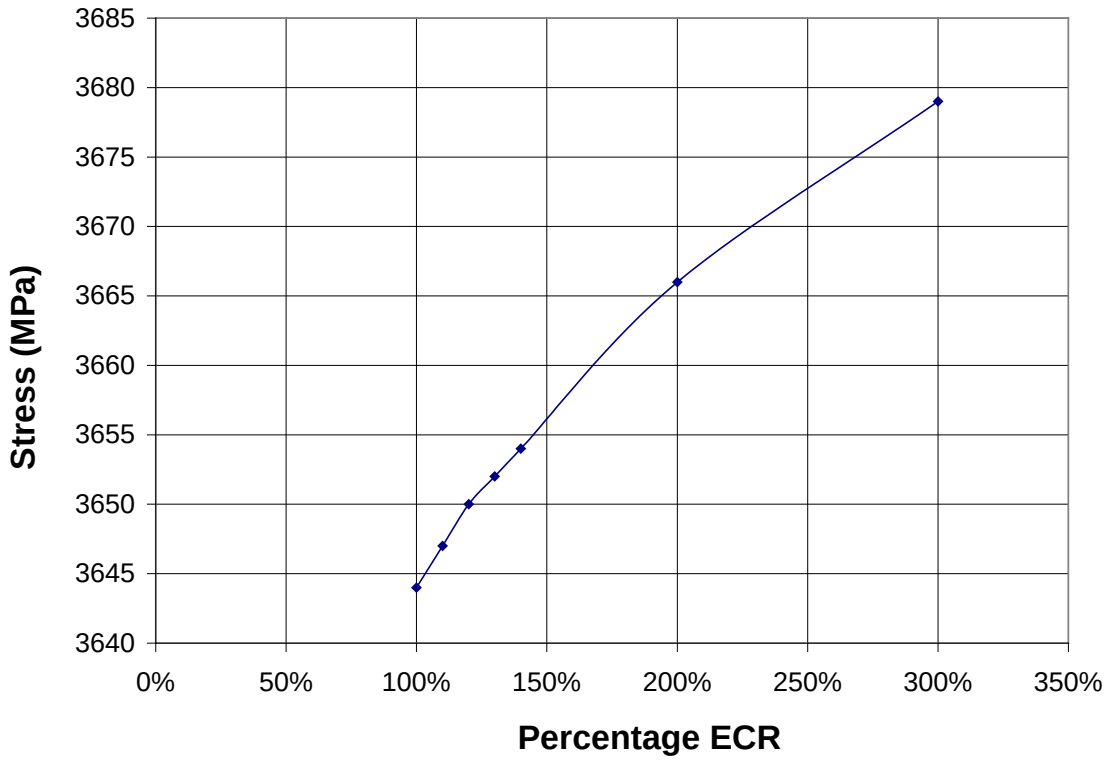

Figure 62 – Maximum von Mises Stress vs. Percentage Increase ECR.

The location of the maximum von Mises stress remains near the axis of symmetry. As the electrical and thermal contact resistances properties increase, von Mises stress, most likely due to thermally induced strain, tends to increase, as shown in Figure 62.

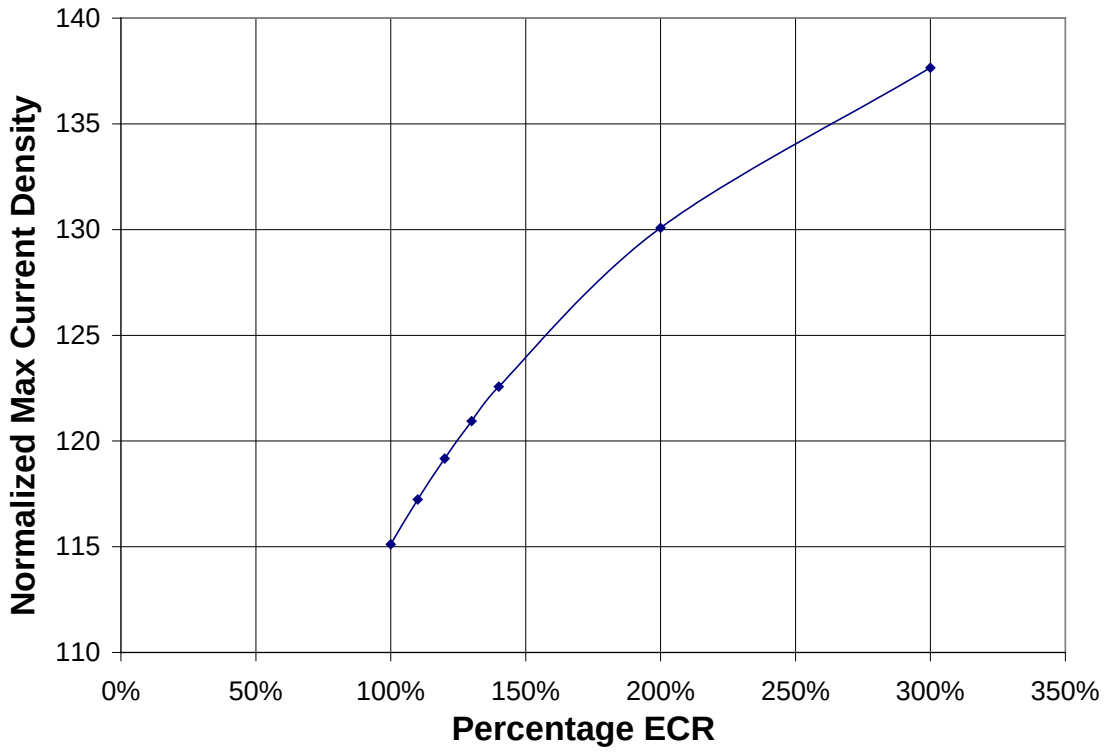

Figure 63 – Normalized Maximum Current Density vs. Percentage Increase ECR.

The location for the normalized maximum current density remains near the contact interfaces. As the electrical and thermal contact resistances properties increase, the normalized maximum current density tends to increase, as shown in Figure 63. As electrical contact resistance is increased at the surfaces in contact, normalized maximum current density increases. Since current is held constant and current density increases, the volume which carries the current through the connector decreases. Again, this could lead to localized hot spots at the micro and nano-scales, which could drastically change the surface morphology and connector resistance.

8.3.3 Comparison of Results of Increasing ECR to Results of Slightly Worn and Failed Connectors

Table 6 – Results for Increasing ECR Properties Compared with Worn and Failed Connector Surfaces

Percentage Increase	T1	Connector Resistance	Maximum von Mises Stress	Normalized Maximum Current Density
100%	113.88	0.059116	3644	115.12
110%	113.94	0.059271	3647	117.24
120%	114	0.059413	3650	119.17
130%	114.06	0.059551	3652	120.94
140%	114.12	0.059676	3654	122.57
200%	114.39	0.060302	3666	130.09
300%	114.72	0.061044	3679	137.65
Slightly Worn	114.52	0.060587	3671	123.97
Failed	114.57	0.060716	3673	124.83

Table 6 shows the results of increasing the electrical and thermal contact resistance properties as compared to the results of running the 3-D multi-physics FEA using the electrical and thermal contact resistance properties from a worn and a failed connector surface. Using predictions for electrical and thermal contact resistance from the worn and failed connector, the results for temperature at Position 1, electrical contact resistance across the connector, and maximum von Mises stress fall between the 200% and 300% increase in electrical and thermal contact resistance predictions of a smooth

connector. Normalized maximum current density falls between 140% and 200% increase in electrical and thermal contact resistance predictions of a smooth connector. Any additional resistance due to chemical degradation is not considered as the multiscale rough surface contact model only deals with the surface profile, not its chemical makeup. As expected, these results would suggest that the electrical and thermal contact resistance properties for the worn and failed connector surfaces are greater than the critical electrical and thermal contact resistance properties.

CHAPTER 9

Conclusions

The work presents a 2-D and 3-D multi-physics FEA to help predict temperature, electric potential, displacement, von Mises stress, and current density distributions in a round pin, high power connector. Several results worth noting stand out from the all simulations run.

9.1 2-D Multi-physics FEA

The 2-D multi-physics FEA was computationally efficient, yielding results in about a tenth of the time that the 3-D multi-physics FEA could. However, the behavior of the results was cause for concern and didn't adequately model all of the phenomena of the connector observed in the lab. As shown, the voltage drop in the 2-D multi-physics FEA tended to be uniform across the entire connector. Bulk resistance should be low across the connector, on both the male and female ends, up to the contact interface. There should then be a concentrated drop in voltage at the two contact interfaces. Results do not show this qualitative behavior.

The reason the contact resistance doesn't mimic what's been found in the experimental results is because of the spring. It is modeled as a composite mass of air and copper. Its main shortcoming is that because of the geometry, contact pressure is uniform across the contact interfaces. In reality, contact is concentrated at three locations, on the two tabs connecting the spring to the female end of the connector and the one tab connecting the spring to the male end of the connector. The 2-D multi-physics FEA was replaced with the 3-D multi-physics FEA because of the geometrical inconsistencies in modeling the round pin high power connector.

9.2 3-D Multi-physics FEA

First, electrical contact resistance trends can be predicted using the model, and with some adjustment of the values, electrical contact resistance values show good correlation to the experimentally measured values. In using the 3-D multi-physics FEA, it was found that the area boundary condition provided a better correlation with the thermal data from the experiment. It was this boundary condition that was employed when determining the results when the ECR was increased.

Second, normalized current density with respect to current is not remaining constant but is increasing after a threshold current has been reached. This suggests that the same path of least resistance is responsible for carrying more and more current as the current increases. This could be problematic as higher currents lead to higher temperatures, especially at the contacting surfaceasperities thus resulting in a more dramatic change in the surface characteristics.

Third, the general trend for current density shows the location of the maximum to be at the interfaces of the spring and the connector parts. It should be expected that the two tab interfaces that connect the spring to the female end of the connector should carry equal currents. However, in Figure 16, one tab carries most of the current. This probably occurs because current flowing through the spring will travel along the path of least resistance. The tabs on the spring probably have similar order of magnitude contact pressures, which would give similar electrical contact resistance.

Fourth, as current increases, maximum von Mises stress remains relatively constant until a critical amperage is reached, somewhere between 75A and 100A. The location of this maximum changes from in the spring to the male end of the connector.

The von Mises stresses calculated in the spring are ten times that of the yield strength of the annealed copper in the spring.

9.3 Increasing ECR

Increasing the electrical and thermal contact resistance properties from the Wilson et al. multiscale model [13] provided a way to model the static multi-physics FEA with some dynamic considerations taken into account. The results also showed at which percentage increase of the electrical and thermal contact resistance properties from the smooth connector would correspond to electrical and thermal contact resistance properties from a worn and failed connector. For increases in ECR and TCR, voltage drop across the connector increased, temperature at Position 1 increased, maximum von Mises stress increased, and normalized maximum current density increased. Using the Wilson et al multiscale method [13] in the 3-D multi-physics FEA, the failed and worn connectors could be shown to have results that lie between a 200% and 300% increase in the smooth connector multiscale properties.

CHAPTER 10

Future Work and Recommendations

A 3-D multi-physics FEA modeling the behavior of a round pin, high power connector was created. The results gathered from the 3-D multi-physics FEA in Chapter 8 corresponded well with the experimental results in Chapter 6. Using a percentage increase of smooth connector multiscale properties and the multiscale properties of a slightly worn and failed connector, some insight may be gathered on how the connector could perform as it neared failure. The following examples of future work are presented in order of apparent difficulty.

The current round pin high power connector uses a silver plating but other finishes could be incorporated. New surface measurements using the profilometer would need to be taken with the new connector finishes. The respective material properties, depending on the new finish, would then need to be changed in the existing model. Running the simulations and experiments would be similar to how they have been lined out in this work. Beyond taking new surface measurements and changing the current material properties, another layer of material could be added to the physical layout of the connector in the FEA. On top of this finish layer, Conta and Target elements would still be used to determine the contact in the 3-D multi-physics FEA; however, the properties entered here would be that of a thin film. This way the existence of oxide layers could be investigated.

Once this work has been completed, the efforts could move to modeling the wear taking place as the connector is vibrated. These connectors operate primarily in hybrid vehicles, which, as they drive down the road, are subjected to random vibration. The

random excitation of the connector causes relative motion between the parts of the connector and thus causes fretting, a contact degradation mechanism, based on wear, which leads to contact failure. Incorporating wear mechanisms into the model should be the next step in the modeling effort. The models should begin by incorporating two of the three parts, namely modeling the wear between the spring and the female end of the connector and between the spring and the male end of the connector. Modeling wear should incorporate the displacement amplitude and vibration frequency. Utilizing these two parameters, the amount material removed with each sweep would need to be calculated, and the geometry of the FEA would need to be recalculated. A pre-determined number of sweeps could be performed and at the end, the contact resistance for the worn geometry could be computed. These results could then be compared to experimental results for the same number of sweeps. Eventually, modeling of the chemical effects of oxidized materials could be included in the fretting models.

References

1. Antler, M., *Electrical effects of fretting connector contact materials: A Review.* Wear, 1985. **106**(1-3): p. 5-33.
2. El Abdi, R., Beloufa, A., Benjemaa, N, *Contact resistance study of high-copper alloys used in power automotive connectors.* Journal of Automobile Engineering, 2007. **222**: p. 1375-1383.
3. Goodman Simon J.N., P.T.F., *The contact resistance and wear behavior of separable contact materials.* Wear, 1989. **131**(1): p. 177-191.
4. Hannel, S., Fouvry, S., Kapsa, Ph., Vincent, L., *The fretting sliding transition as a criterion for electrical contact performance.* Wear, 2001. **249**: p. 761-770.
5. Jedrzejczyk, P., Fouvry, S., Chalandon, P., *A fast methodology to quantify electrical-contact behaviour under fretting loading conditions.* Wear, 2009. **267**: p. 1731-1740.
6. Lee, S., Cho, H., Jang, Y.H., *Multiscale electrical contact resistance in clustered contact distribution.* Journal of Physics, 2009. **42**: p. 1-7.
7. Malucci, R.D. *Fretting Corrosion Degradation, Threshold Behavior and Contact Instability*. in *Proceedings of 49th IEEE Holm Conference Electrical Contacts*. 2003. Washington, D.C.
8. McBride, J.W., *The relationship between surface wear and contact resistance during the fretting of in-vivo electrical contacts.* IEEE Transactions on Components and Packaging Technologies, 2008. **30**(3): p. 592-600.
9. Park, Y.W., Narayanan, T.S.N. Sankara, Lee, K.Y., *Effect of temperature on the fretting corrosion of tin plated copper alloy contacts.* Wear, 2007. **262**: p. 320-330.
10. Park, Y.W., Bapu, G.N.K. Ramesh, Lee, K.Y., *The influence of current load on fretting of electrical contacts.* Tribology International, 2008. **42**: p. 682-689.
11. Swingler, J., McBride, J.W., *Fretting corrosion and the reliability of multicontact connector terminals.* IEEE Transactions on Components and Packaging Technologies, 2002. **25**(4): p. 670-676.
12. Tristani, L., Zindine, E.M., Boyer, L., Klimek, G., *Mechanical modeling of fretting cycles in electrical contacts.* Wear, 2001. **249**: p. 12-19.
13. Wilson, W.E., Angadi, Santosh V, Jackson, Robert L., *Surface separation and contact resistance considering sinusoidal elastic-plastic multi-scale rough surface contact.* Wear, 2010. **268**: p. 190-201.
14. Holm, R., *Electrical Contacts, Theory, and Applications*, in *Springer-Verlag*. 1967: Berlin.
15. Bowden, F.P., Williamson, J.B.P., *Electrical conduction in solids I. Influence of the passage of current on the contact between solids.* Proceedings of Royal Society of London. Series A, Mathematical and Physical Sciences, 1958. **246**: p. 1-12.
16. Greenwood, J.A. and J.B.P. Williamson, *Electrical Conduction in Solids. II. Theory of Temperature-Dependent Conductors.* Proceedings of the Royal Society of London. Series A, Mathematical and Physical Sciences, 1958. **246**(1244): p. 13-31.

17. Greenwood, J.A. and J. Harris, *Electrical Conduction in Solids. III. The Contact of Iron Surfaces.* Proceedings of the Royal Society of London. Series A, Mathematical and Physical Sciences, 1963. **257**(1288): p. 83-97.
18. Bruel, J.F., Smirou, P., Carballeira, A. *Gas environment effect on the fretting corrosion behaviour of contact materials*. in *Proceedings of 14th ICEC*. 1988. Paris, France.
19. van Dijk, P., Rudolphi, A.K., Klaffke, D., *Investigations on Electrical Contacts Subjected to Fretting Motion.*
20. Rudolphi, A.K., Jacobson, S., *Gross plastic fretting mechanical deterioration of silver coated electrical contacts.* Wear, 1996. **201**: p. 244-254.
21. Bansal, D.G., Streator, J. L. *Voltage saturation in electrical contacts*. in *ASME/STLE 2009 International Joint Tribology Conference*. 2009. Memphis, TN: IJTC.
22. Ciavarella, M., Murolo, G., Demelio, G., *The electrical/thermal conductance of rough surfaces - the Weierstrass-Archard multiscale model.* International Journal of Solids and Structures, 2004. **41**: p. 4107-4120.
23. Gallego, L., Nelias, D. *Modeling of fretting wear under gross slip and partial slip conditions*. in *STLE/ASME International Joint Tribology Conference*. 2007. San Antonio, TX.
24. Kogut, L., Etsion, I., *Electrical Conductivity and Friction Force Estimation in Compliant Electrical Connectors.* Tribology Transactions, 2000. **43**(4): p. 816-822.
25. Jang, Y.H., Barber, J.R., *Effect of contact statistics on electrical contact resistance.* Journal of Applied Physics, 2003. **94**(11): p. 7215-7221.
26. Noyes, D., Green, I. *Finite element analysis of structural and electromagnetic effects on asperity contacts*. in *ASME/STLE International Joint Tribology Conference*. 2009. Memphis, TN.
27. Greenwood, J.A., Williamson, J.B.P., *Contact of Nominally Flat Surfaces.* Proceedings of Royal Society of London, 1966. **295**: p. 300-319.
28. McColl, I.R., Ding, J., Leen, S.B., *Finite element simulation and experimental validation of fretting wear.* Wear, 2004. **256**: p. 1114-1127.
29. Ding, J., McColl, I.R., Leen, S.B., Shipway, P.H., *A finite element based approach to simulating the effects of debris on fretting wear.* Wear, 2007. **263**: p. 481-491.
30. Ossart, F., Noel, S., Alamarguy, D., Correia, S., Gendre, P., *Multilayer contacts in electrical connectors: experimental results and modelling.* WIT Transactions on Engineering Sciences, 2007. **55**: p. 89-110.
31. Chang, W.R., Etsion, I., Bogy, D.B., *An Elastic-Plastic Model for the Contact of Rough Surfaces.* ASME Journal of Tribology, 1987. **109**(2): p. 257-263.
32. Jackson, R.L., Green, I., *A Statistical Model of Elasto-plastic Asperity Contact between Rough Surfaces.* Tribology International, 2006. **39**(9): p. 906-914.
33. Kogut, L., Jackson, R.L., *A Comparison of Contact Modeling Utilizing Statistical and Fractal Approaches.* ASME Journal of Tribology, 2005. **128**(1): p. 213-217.
34. Majumdar, A., Bhushan, B., *Fractal Model of Elastic-plastic Contact Between Rough Surfaces.* ASME Journal of Tribology, 1991. **113**(1): p. 1-11.

35. Bora, C.K., et al, *Multiscale Roughness and Modeling of MEMS Interfaces.* Tribology Letters, 2005. **19**(1): p. 37-48.
36. Jackson, R.L., Streator, J.L., *A Multiscale Model for Contact between Rough Surfaces.* Wear, 2006. **261**(11-12): p. 1337-1347.
37. Johnson, K.L., Greenwood, J.A., Higginson, J.G., *The Contact of Elastic Regular Wavy Surfaces.* Int. J. Mech. Sci, 1985. **27**(6): p. 383-396.
38. Krithivasan, V.L., Jackson, R.L., *An Analysis of Three-Dimensional Elasto-Plastic Sinusoidal Contact.* Tribology Letters, 2007. **27**(1): p. 31-43.
39. Jackson, R.L., Krithivasan, V.L., Wilson, W.E., *The Pressure to Cause Complete Contact between Elastic Plastic Sinusoidal Surfaces.* Proceedings of the Institution of Mechanical Engineers, Part J: Journal of Engineering Tribology. **222**(7): p. 857-863.
40. Angadi, S.V., Wilson, W.E., Jackson, R.L., Flowers, G.T., Rickett, B.I. *A multi-physics finite element model of an electrical connector considering rough surface contact*. in *The 54th IEEE Holm Conference on Electrical Contacts*. 2008. Orlando, Fl.